ANKARA YILDIRIM BEYAZIT UNIVERSITY

GRADUATE SCHOOL OF NATURAL AND APPLIED SCIENCES


# ZnO COATING ON KEVLAR™ FABRICS BY HYDROTHERMAL METHOD AND INVESTIGATION OF GAS SENSOR PROPERTIES

**Ph. D. Thesis by**

**Bahadır AYDAŞ**

**Department of Materials Engineering**

**July, 2024**

**ANKARA**

# ZnO COATING ON KEVLAR™ FABRICS BY HYDROTHERMAL METHOD AND INVESTIGATION OF GAS SENSOR PROPERTIES

**A Thesis Submitted to**

**The Graduate School of Natural and Applied Sciences of**

**Ankara Yıldırım Beyazıt University**

**in Partial Fulfillment of the Requirements for the Degree of Doctor of Philosophy of Science in Materials Engineering**

**by**

**Bahadır AYDAŞ**

**July, 2024**

**ANKARA**

## Ph. D. THESIS EXAMINATION RESULT FORM

We have read the thesis entitled **"ZnO COATING ON KEVLAR™ FABRICS BY HYDROTHERMAL METHOD AND INVESTIGATION OF GAS SENSOR PROPERTIES"** completed by **BAHADIR AYDAŞ** under the supervision of **ASSOC. PROF.DR. MEHMET FATİH ÖKTEM** and **DR. ABDULLAH ATILGAN** and we certify that in our opinion it is fully adequate, in scope and in quality, as a thesis for the degree of Doctor of Philosophy.

| | |
|---|---|
| Assoc. Prof. Dr. Mehmet Fatih ÖKTEM | Dr. Abdullah ATILGAN |
| Supervisor | Co-Supervisor |
| Assoc. Prof. Dr. Gülsüm TOPATEŞ | Prof. Dr. Abdullah YILDIZ |
| Jury Member | Jury Member |
| Assoc. Prof. Dr. Elmas SALAMCI | Assoc. Prof. Dr. Hanifi ÇİNİCİ |
| Jury Member | Jury Member |

Prof. Dr. Sadettin ORHAN

Director

Graduate School of Natural and Applied Sciences

# ETHICAL DECLARATION

I hereby declare that, in this thesis which has been prepared in accordance with the Thesis Writing Manual of Graduate School of Natural and Applied Sciences,

- All data, information and documents are obtained in the framework of academic and ethical rules,
- All information, documents and assessments are presented in accordance with scientific ethics and morals,
- All the materials that have been utilized are fully cited and referenced,
- No change has been made on the utilized materials,
- All the works presented are original,

and in any contrary case of above statements, I accept to renounce all my legal rights.

**Date:** 04.07.2024 **Signature:……..**

**Name & Surname: Bahadır AYDAŞ**

# ACKNOWLEDGMENTS

I dedicate my deepest thanks to my supervisors, Assoc. Prof. Dr. Mehmet Fatih ÖKTEM and Dr. Abdullah ATILGAN, for their advice, patience and great understanding during the development and completion of this thesis.

In addition to my advisors, I would like to thank the rest of my thesis committee members: Prof. Dr. Abdullah YILDIZ, Assoc. Prof. Gülsüm TOPATEŞ, Assoc. Prof. Dr. Elmas SALAMCI and Assoc. Prof. Dr. Hanifi ÇİNİCİ for their encouragement and insightful comments.

I am also thankful to Prof. Dr. Selim ACAR, Dr. Ahmad AJJAQ and Research Assistant İremnur AKÇAKOCA for their supports, laboratory facilities and numerous helpful discussions during my thesis work.

Most of all, I want to thank my family, my wife Hilal and my lovely daughter Sare for their always support, encouragement and trust. Without their support, none of this would have been possible.

**2024, July** **Bahadır AYDAŞ**

# ZnO COATING ON KEVLAR™ FABRICS BY HYDROTHERMAL METHOD AND INVESTIGATION OF GAS SENSOR PROPERTIES

## ABSTRACT

Owing to their nanostructure morphology, flexibility and high thermal resistance, Kevlar fabric substrates are an ideal candidate for obtaining flexible gas sensors for particularly new-generation wearable technologies. The morphology of the surface of the substrate where the target gas comes into contact directly affects the important features of the sensor such as detection limit, selectivity, and response. Here, a practical method for improving the performance of flexible gas sensors based on Zinc Oxide/Kevlar is proposed, which involves adjusting the morphology of Zinc Oxide. Zinc Oxide based gas sensing layers were deposited on Kevlar fabric substrates by a two-stage method. Firstly, a seed layer was produced on Kevlar using the ultrasonic bath method, with five different seed layer processing times ranging from 1 minute to 20 minutes. In the nucleation step, then, all nanostructured layers were deposited by hydrothermal method with constant parameters and under the same experimental conditions. As the seeding time was increased, the nanorods (1 Dimensional) formed on the surface became flakes (2 Dimensional), leading to a considerable improvement in ammonia gas sensing properties. The sensor with a 5-minutes seeding time showed a sensitivity of 49 percent at an optimal operating temperature of 190 °C, while the sensor produced in 20 minutes showed the best response performance with 169 percent at 130 °C for 50 ppm ammonia gas. The increase in seeding time not only reduced the operating temperature of the gas sensor through the conversion from 1 Dimensional nanostructure to 2 Dimensional, but also significantly increased the sensor response. Under constant hydrothermal method conditions and solution concentration, the density per unit area increases. However, after 10 minutes of seeding, the length of nanorods shortens and turn into a rod-flake hybrid morphology. Having set that a superior sensor performance is demonstrated for the investigated samples. The obtained results also showed that flexible Kevlar fabric could be a feasible and interesting substrate for nanostructured Zinc Oxide-based ammonia gas sensors.

**Key Words:** Zinc Oxide, Ammonia Gas Sensors, Seed Layer, Hydrothermal Synthesis, Kevlar Fabric, 1D and 2D nanostructures

# KEVLAR™ KUMAŞLAR ÜZERİNE HİDROTERMAL YÖNTEMLE ZnO KAPLAMA VE GAZ SENSÖR ÖZELLİKLERİNİN İNCELENMESİ

## ÖZ

Kevlar kumaş yüzeyleri, nanoyapı morfolojileri, esneklikleri ve yüksek termal dirençleri sayesinde, özellikle yeni nesil giyilebilir teknolojilerde esnek gaz sensörleri elde etmek için ideal bir adaydır. Hedef gazın temas ettiği substrat yüzeyinin morfolojisi, sensörün algılama limiti, seçiciliği ve tepkisi gibi önemli özelliklerini doğrudan etkiler. Bu çalışmada, Çinko Oksit/Kevlar bazlı esnek gaz sensörlerinin performansını artırmak için Çinko Oksit morfolojisinin ayarlanmasını içeren pratik bir yöntem önerilmektedir. Çinko Oksit bazlı gaz algılama katmanları, iki aşamalı bir yöntem ile Kevlar kumaş yüzeyine kaplanmıştır. İlk olarak Kevlar üzerinde ultrasonik banyo yöntemi kullanılarak 1 dakikadan 20 dakikaya kadar beş farklı işlem süresine sahip tohum katmanı üretilmiştir. Çekirdeklenme adımında, tüm nanoyapılı katmanlar hidrotermal yöntem ile sabit parametrelerle ve aynı deneysel koşullar altında büyütülmüştür. Tohumlama süresi arttıkça yüzeyde oluşan nanoçubuklar (1 Boyutlu) pullara (2 Boyutlu) dönüşmüş ve bu da amonyak gazı algılama özelliklerinde önemli bir iyileşmeye olanak sağlamıştır. 5 dakika tohumlama süresine sahip sensör, 190 °C optimum çalışma sıcaklığında yüzde 49 hassasiyet gösterirken, 20 dakikada üretilen sensör, 50 ppm amonyak gazı için 130 °C'de yüzde 169 ile en iyi tepki performansını göstermiştir. Tohumlama süresindeki artış, 1 Boyutlu nanoyapıdan 2 Boyutluya dönüşüm yoluyla yalnızca gaz sensörünün çalışma sıcaklığını düşürmekle kalmamış, aynı zamanda sensör yanıtını da önemli ölçüde artırmıştır. Sabit hidrotermal yöntem koşulları altında ve aynı çözelti konsantrasyonuyla birim alan başına yoğunluk artmıştır. Ancak 10 dakikalık tohumlama işlemleminden sonra nanoçubukların uzunluğu kısalmış ve çubuk-pul hibrit morfolojisine dönüşmüştür. İncelenen numuneler için üstün bir sensör performansı ortaya konmuştur. Elde edilen sonuçlar ayrıca esnek Kevlar kumaşın nanoyapılı Çinko Oksit bazlı amonyak gazı sensörleri için uygulanabilir ve ilginç bir alttaş olabileceğini göstermiştir.

**Anahtar Kelimeler:** Çinko Oksit, Amonyak Gazı Sensörleri, Tohum Katmanı, Hidrotermal Sentez, Kevlar Kumaş, 1B ve 2B nanoyapılar

**CONTENTS**

# NOMENCLATURE

**Abbreviations**

| | |
|---|---|
| Å | Angstrom |
| eV | Electronvolt |
| J | Joule |
| M | Molarity |
| C | Carbon |
| B | Boron |
| H | Hydrogen |
| O | Oxygen |
| P | Phosphorus |
| W | Tungsten |
| Al | Aluminum |
| Cu | Copper |
| In | Indium |
| Nb | Niobium |
| Si | Silicon |
| ZnO | Zinc oxide |
| CdO | Cadmium oxide |
| CuO | Copper (II) oxide |
| CO | Carbon monoxide |
| NaOH | Sodium hydroxide |
| $SnO_2$ | Tin oxide |
| $In_2O_3$ | Indium oxide |
| $WO_3$ | Tungsten trioxide |
| $TiO_2$ | Titanium dioxide |
| $Al_2O_3$ | Aluminum oxide |
| $Fe_2O_3$ | Iron (III) oxide |
| $NH_3$ | Ammonia |
| $NO_2$ | Nitrogen dioxide |
| $H_2S$ | Hydrogen sulphite |

**Acronyms**

| | |
|---|---|
| UV | Ultraviolet |
| MOS | Metal oxide semiconductor |
| ppm | Part per million |
| nm | nanometer |
| AFM | Atomic force microscope |
| XRD | X-Ray diffraction |
| 1D | One dimensional |
| 2D | Two dimensional |
| PEI | Poltethyleneimine |
| DI | Deionized |
| DT | Interdigital transducer |
| SEM | Scanning electron microscopy |
| AE | Acetone |
| EtOH | Ethanol |
| RT | Room temperature |
| FHWM | Full width at half maximum |
| EDL | Electron depletion layer |
| MFC | Mass flow controller |
| EDS | Energy dispersive x-ray spectroscopy |
| PPTA | Poly (p-phenylene terephthamide) |

# LIST OF TABLES

# LIST OF FIGURES

# CHAPTER 1

# INTRODUCTION AND LITERATURE REVIEW

## 1.1 Semiconductor Materials

Crystalline solids whose electrical conductivity properties lie between insulating materials and conductive materials are called semiconductors. The conductivity properties of semiconductors vary depending on the movement of electrons. When the conduction of electric current is examined according to electron movement, the substances can be evaluated under three main headings. While conductive materials show the smallest resistance to electric current, insulating materials show the highest resistance. Semiconductors, on the other hand, can exhibit both insulating and conducting properties depending on environmental variables. In semiconductors, there are resistances and energy gaps that exist between the values of conducting materials and insulating materials [1].

In order to better understand the terms conductor, insulator and semiconductor, it is necessary to examine materials at the atomic level. In general, the components of the atom, which is the smallest building block of matter, can be said to be neutrons, protons and electrons. Conductivity and insulation mechanisms are also mechanisms that depend on the movement of these particles of the atom. When we look at the structure of the atom, it is stated that there are neutrons and protons in its centre and electrons move around this centre. The atomic model and structure is shown in Fig. 1.1. The electrical conductivity behaviour of a material depends on the movement of these electrons. As these negatively charged particles move around the nucleus of the atom, they are subjected to the attraction force of the nucleus. At the same time, it is exposed to centrifugal force due to its rotation movement and continues its movement in balance with these two forces. The fact that electrons are in constant motion ensures that they have a certain energy level. Thanks to this balance and energy, electrons rotate in an orbit around the atomic nucleus. If an effect is applied to the electrons due to external factors and an energy above their current level is applied, the electrons leave

their current orbit and move to a higher orbit. In general, the arrangement of neutrons, protons and electrons in the atomic structure is as described above [2].

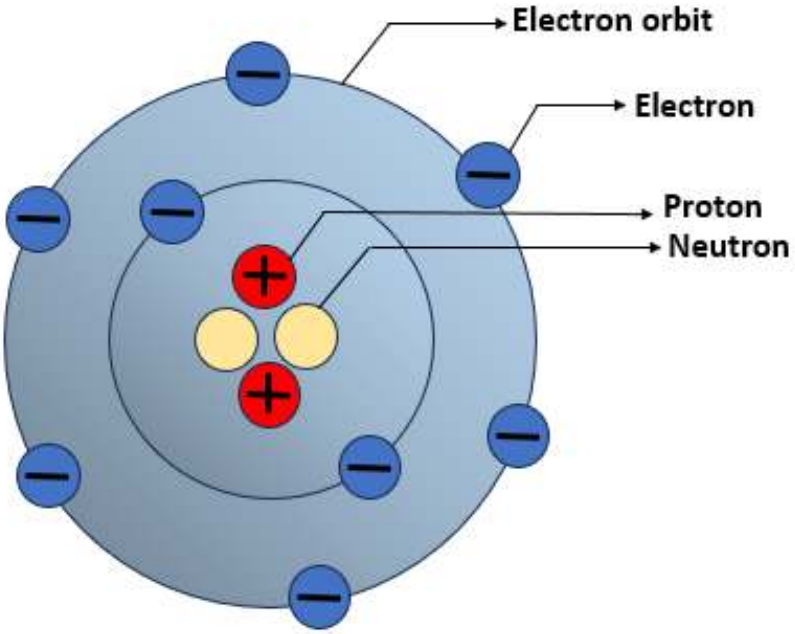


**Figure 1.1** Atomic model and structure.

Electrons that called valence electrons are located in the outermost orbit of an atom. The last orbital where these electrons are located is called the valence orbital. Just as the electrons in each orbital have their own energy, the valence electrons in this last orbital also have their own energy. This energy is called valence band energy. Based on these definitions, in order for a material to become conductive, electrons must jump from the valence band to the conduction band. The energy required for this jump is the conduction band energy and is the amount of energy required to remove the electron in the valence band from the atom [3]. Energy band gaps of materials according to their conductivity properties are shown in Fig. 1.2.

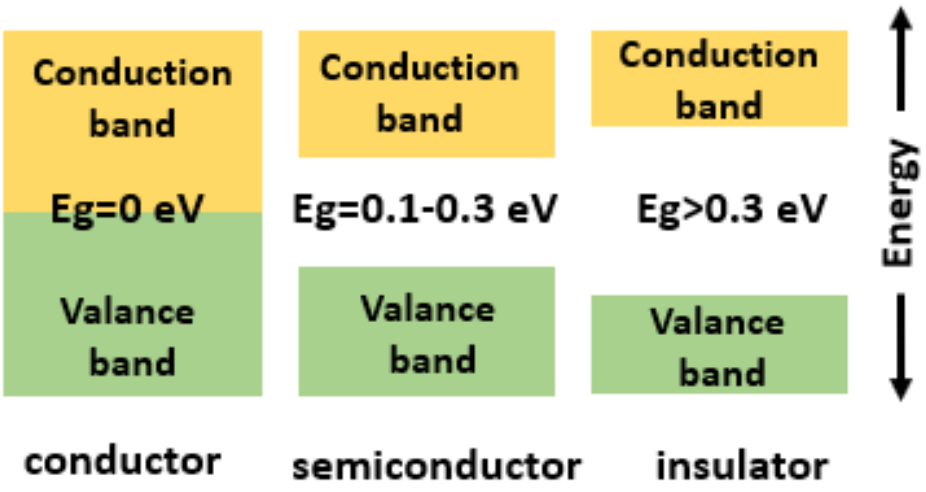


**Figure 1.2** Energy band gaps of materials.

The source of the current passing through the materials is the electron transfer from the valence band to the conduction band. The conductivity properties of a material are directly related to the gap between these two bands. As the band gap increases, the conductivity decreases, and as the band gap decreases, the conductivity also increases. In conductive materials, there is generally no gap between the valence band and the conduction band. For this reason, in conductive materials, a very low level of energy is sufficient for the valence electrons to become free. In semiconductors, the energy required for the electron in the valence band to become free is relatively higher. The energy level supplied externally must be at least as much as the gap between the valence band and the conduction band. When the gap between these two bands in insulating materials is too large, the energy given from the outside must be at a much higher level. The type of energy required may be heat, magnetic, electrical or light energy [4].

The band gap mentioned above is also known as the forbidden energy and the energy difference between the valence band and the conduction band is expressed as electron volts (eV). One eV is used as the energy unit to describe the energies of electrons. One eV is the amount of energy an electron gains by crossing a potential difference of one volt. In other words, it is the amount of kinetic energy obtained by accelerating a single electron with a potential difference of one volt. eV is approximately $1.602 \times 10^{-19}$ joules

(J), used to describe the energy of subatomic particles in semiconductor, solar cells, particle physics, or other electronics fields of study [5].

Another mechanism that can change the electrical conductivity properties of semiconductor materials is the addition of certain amounts of different atoms into the material. Small amounts of different atoms added into the material can significantly change the electrical properties of semiconductors. These atoms, called impurity atoms, are placed in the crystal in amounts and methods that will not disrupt the structure and character of the semiconductor material. These processes are called doping [6]. An example of this phenomenon is the doping process on silicon crystal. The atomic number of the silicon crystal is 14, and the bonds with neighbouring atoms are determined by the 4 electrons in the outermost orbit. These 4 electrons form the basic structure of the silicon crystal by creating covalent bonds with four different silicon atoms. By repeating these structures, silicon (Si) crystals are formed [7]. The arrangement of silicon atoms is shown in Fig. 1.3.

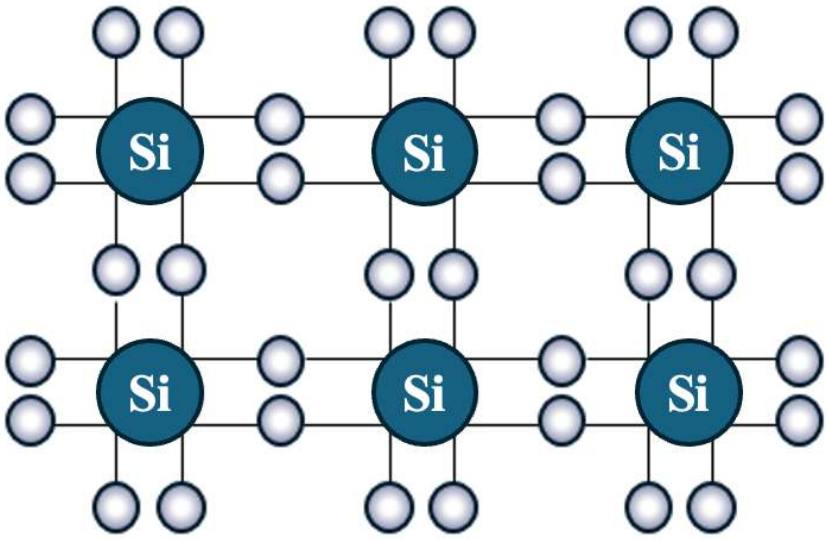


**Figure 1.3** Arrangement of silicon atoms.

Semiconductors, which generally exist in crystalline structures, are a transition type between insulators and conductors in terms of band gap. In semiconductors, within a

certain temperature range, unlike metals, resistivity decreases as the temperature increases [8]. Semiconductors are used to control electric current in electronic devices due to the change in conductivity properties. As the simplest examples, we encounter semiconductors in the working mechanism of phones and computers. In addition, semiconductors play a role in the conversion of solar energy into electrical energy in solar cell cells. Since the electrical properties of semiconductors can be controlled, these materials can increase the performance efficiency in devices. From this perspective, progress in many technological fields is directly related to semiconductors. Semiconductors, which can be recycled and are in the class of pure solid materials, have a wide range of usage in chemistry and solid-state physics studies [9]. The atoms of the crystals of semiconductor materials are in a covalently bonded structure under normal conditions and do not have free electrons. The conductivity levels of these materials, whose crystal structure is so regular, can be increased with certain additives. Depending on the type of dopant, two different types of semiconductors are created: P-type and N-type [10].

### 1.1.1 P-type Semiconductors

Conduction of electric current in semiconductors occurs by the movement of free electrons and holes. P-type semiconductors are obtained by adding dopants that create gaps in the valence band to the material structure. These holes carry positively charged electric current, and in P-type semiconductors, holes act as majority carriers and electrons act as minority carriers [11].

P-type semiconductor material can be created by doping materials such as Boron (B), Aluminium (Al) or Indium (In) to a pure semiconductor material such as silicon or germanium. [12]. Structure of silicon crystalline doped with B atom is shown in Fig. 1.4. With this process, the purity level of the pure semiconductor decreases. In this example, a P-type semiconductor was obtained by adding B atoms to crystals with 4 electrons in the valence orbits. In this case, the added impurities have one less valence electron than the atoms of the semiconductor. For this reason, an electron gap occurs in the newly formed structure, which causes the P-type semiconductor to be a positive charge carrier [11].

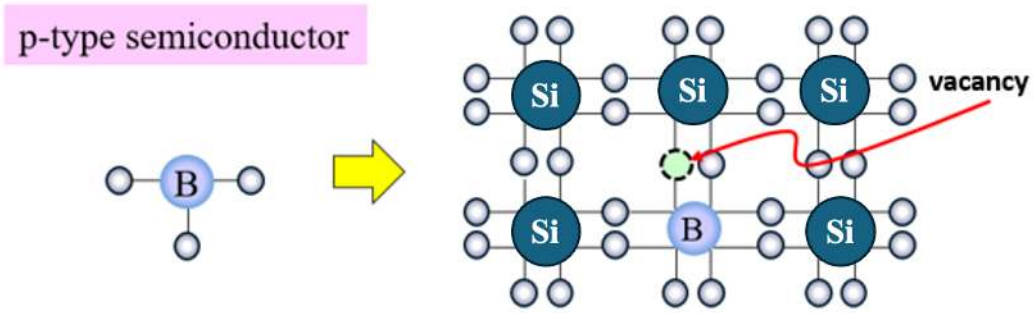


**Figure 1.4** Structure of B doped silicon crystal.

As a result, to explain with the same example, if element B is added to the Si element, Si atoms and 3 electrons of element B form a covalent bond and a 1-electron gap is created in the crystal structure. One of the electrons of the neighbouring atom in the structure can come into this gap with a low level of energy. Thus, a gap may form in the valence band with an energy lower than the forbidden energy gap.

Various devices such as diodes, transistors, and solar cells are used with P-type semiconductors. A P-N junction is formed by combining a P-type semiconductor with an N-type semiconductor. In this connection, the P-type forms the anode part or the positive part. When voltage is applied to this junction, the holes of the P-type semiconductor pass to the N-type semiconductor, and the excess electrons in the N-type semiconductor pass to the P-type semiconductor, creating a neutral depletion region. In this way, a potential obstacle that controls the flow occurs in the device used [13].

### 1.1.2 N-Type Semiconductors

N-type semiconductors are a type of semiconductor that has an extra electron in the conduction band, unlike P-type semiconductors. These electrons, which serve as negatively charged carriers of the electric current, are also included in the crystal structure through the doping process. In the conduction mechanism of the N-type semiconductor, electrons mostly act as carriers, unlike the P-type semiconductor, and positively charged holes are in the minority [14].

To better understand the formation mechanism and structure of an N-type semiconductor, the Si crystal example can be given again. As mentioned before, pure Si atoms are covalently bonded with neighbouring Si atoms. In this crystal structure system, all electrons are included in the bond structure via covalent bonds. In order for an electron to move into the conduction band, energy equal to or greater than the forbidden energy band gap is required. Doping aims to reduce this energy level. For the Si crystal example, group V elements can be used as doping atoms. This is because there are 5 electrons in their final orbits. For example, when the Si crystal is doped with Phosphorus (P) atom, 4 of the 5 electrons in the valence band of phosphorus form covalent bonds with Si atoms. As a result, the remaining 1 electron is bound to the Si atom with a weak electrostatic force and can be removed from there with a low level of energy. Because this electron is weakly bonded to the Si atom, it can break away with much less energy than the energy required to knock off the leading Si atom's electrons. In this system, no hole is formed after the electron passes from the valence band to the conduction band with a low energy. Here P atom is the donor atom. In N-type semiconductors, the atoms given by doping have 1 more valence electron than the semiconductor. Therefore, excess electrons are formed in the structure and negative charge carrier behaviour is observed in the N-type semiconductor. The N-type semiconductor Si atom doped with P is shown in Fig. 1.5 [15] [16].

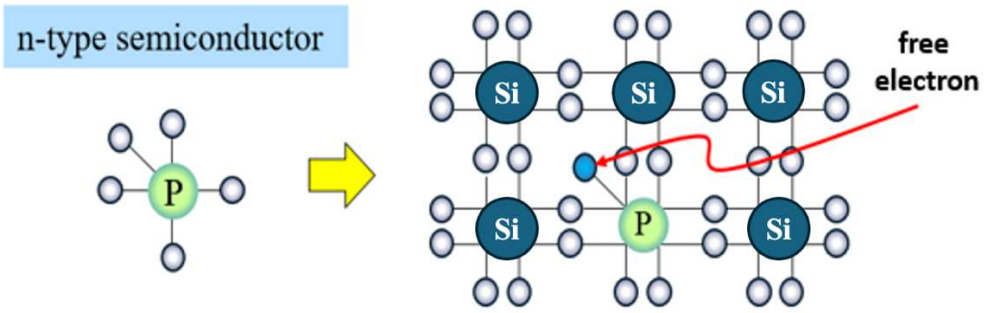


**Figure 1.5** Structure of P doped Si crystal.

## 1.2 Metal Oxides

Chemical compounds formed when metal elements combine and react with oxygen in the air are called metal oxides. Metal oxides can also be synthesized through chemical reactions and are used and advantageous in many applications thanks to their specific properties. The properties of this material depend on the type of metal and its oxidation state. Zinc oxide (ZnO), Cadmium oxide (CdO), Tin oxide ($SnO_2$), Indium oxide ($In_2O_3$), Tungsten trioxide ($WO_3$), Titanium dioxide ($TiO_2$), Copper (II) oxide (CuO), Aluminium oxide ($Al_2O_3$), Iron (III) oxide ($Fe_2O_3$) are the main types of metal oxides.

### 1.1.3 Zinc Oxide (ZnO)

This type of metal oxide, shown with the formula ZnO, is an inorganic compound consisting of zinc and oxygen. ZnO exists in nature in three different crystal structures: Wurtzite, rocksalt and zinc blende. When these three crystal structures were examined from a thermodynamic perspective, it was seen that the most stable structure was Wurtzite. In this structure, 4 oxygen atoms and each zinc atom show a tetrahedral formation. ZnO crystal structures are shown in Fig. 1.6. This water-insoluble compound exists as a white powder. ZnO is a metal oxide with a wide band gap and high electron mobility, located in the near-UV spectral region (≥3.37 eV) and is highly advantageous metal oxide due to its thermal stability, chemical stability, and electromechanical coupling [17]. ZnO is a direct wideband gap optoelectronic semiconductor material that displays many outstanding qualities when used in electronic and optoelectronic devices. ZnO offers a great deal of advantages such as radiation resistance, thermal stability, and biocompatibility. Furthermore, it is possible to create alloys with adjustable band gaps using ZnO and the materials used for its production are relatively easy to acquire [18] [19]. In the synthesis phase, ZnO can be produced and coated in many morphologies in order to provide usage efficiency. This is one of the reasons why ZnO is used especially in gas sensor technology. ZnO can have different morphologies such as nanorod, nanowire, nanobelt, nanoflower and nanoflake. Considering all these features, ZnO appears as a type of metal oxide semiconductor (MOS) material that finds wide use in gas sensors [20].

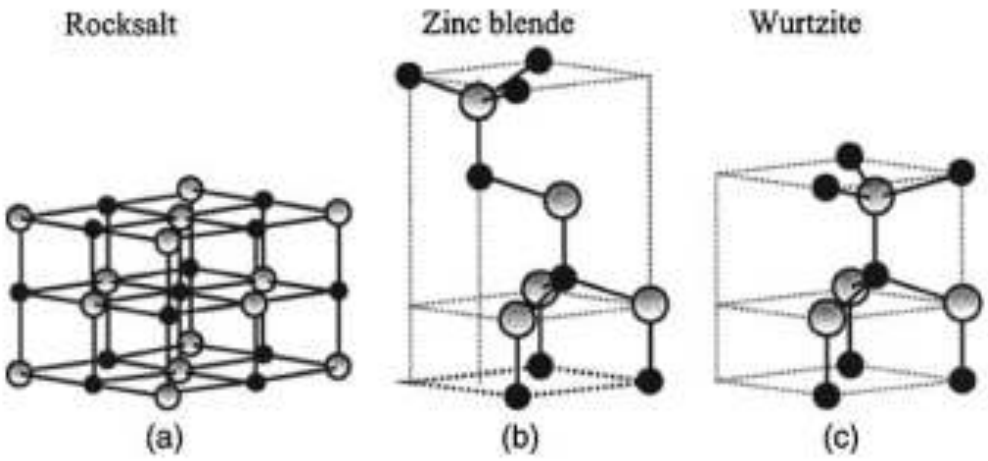


**Figure 1.6** ZnO crystal structures [21].

ZnO is a metal oxide used in the production of glass, ceramics, plastic, rubber and many other materials. It is also used as a pigment in paint applications and as a UV absorber in various cosmetics and personal care products. ZnO, which has antimicrobial properties, is a good conductor and acts as a catalyst in some chemical reactions. Non-toxic, affordable, and chemically stable, ZnO is a biocompatible material. For this reason, it can also be used in medical studies and implant applications.

## 1.3 Gas Sensors

Smart textiles, which emerged as a result of studies in the field of wearable technologies, make life easier in many areas. First of all, it has a wide usage area in health industries, military, sports applications and in general in the fields of electronic applications like sensors and biosensors [22]. Unlike traditional textiles, these materials can sense and respond to ambient conditions [23]. Smart textiles can be examined in two groups as active and passive. Active smart textiles detect stimulus and respond using a sensor mechanism, whereas passive ones perceive environmental stimulus and change their state accordingly [24]. Gas sensors are also an area with development potential in wearable technology.

Gas sensors are electronic devices designed to detect, measure and identify various gases. These sensors are used to detect, monitor or control the presence of gases in

industrial, domestic, medical and environmental applications. The basic gas sensor and its structure are shown in Fig. 1.7. Gas sensors can often be designed specifically for a particular type of gas or can be generally in the form of multiple gas sensors that can detect a variety of gases. In other words, it is a type of chemical sensor that can convert the chemical information of a low concentration gas or gas compound into a signal that can be read by another detector system. This chemical information is obtained as a result of a reaction or change of a physical property in the sensor.

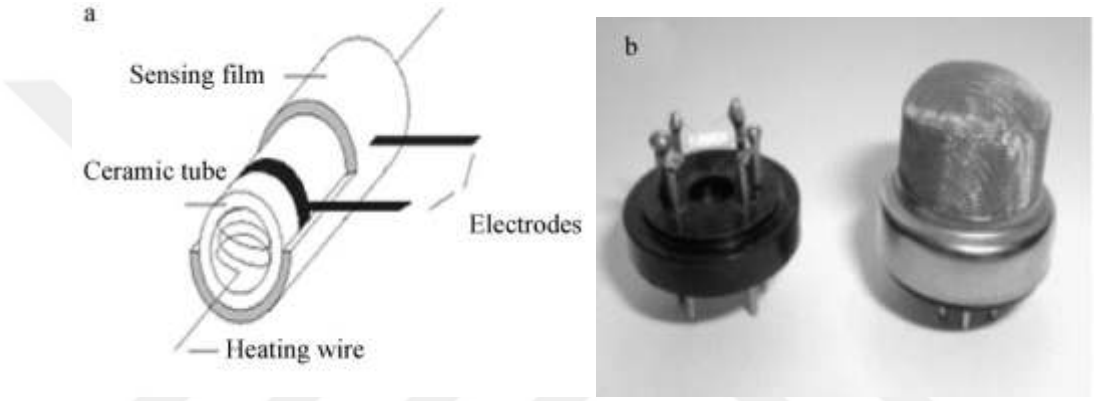


**Figure 1.7**: Structure of gas sensor a) internal sensor mechanism b) external structure [25].

In recent years, with the increasing population and the development of many industrial areas, the increase in air pollution continues to accelerate. Harmful gases released as a result of activities in areas such as the transportation industry, heavy industry, mining and energy production that we are exposed to in daily life have reached levels that directly affect human life negatively, in addition to disrupting balance of nature [26]. In order to prevent this situation, it is necessary to determine the emission amounts of these harmful gases and take precautions by monitoring these amounts in a controlled manner. Gas sensors are devices that play a vital role at this stage, basically detecting the gases in the environment and displaying information about the types and quantities of these gases. Many types of harmful gases can be colorless, odorless and can cause serious harm even at low concentrations. For this reason, studies on gas sensor development continue [27]. When we look at the technologies of the past years in the

field of gas sensors, systems such as gas chromatography/mass spectroscopy and Fourier transform infrared spectroscopy have been used, especially in industrial applications, thanks to their fast response times and high detection capacities. However, these systems have disadvantages such as expensiveness, low thermal resistance, not being portable, and requiring periodic maintenance. Considering all these disadvantages, researchers have conducted many studies on sensors that are portable, can measure in wide temperature ranges, have high thermal resistance, and offer improved selectivity, sensitivity and response time [28].

According to their working mechanisms, we can basically talk about physical, chemical and biochemical sensors. The signal obtained in physical sensors occurs when the properties of the material, such as mass, conductivity and temperature, change. In chemical sensors, data is obtained as a result of the chemical reaction of the substance to be detected with the sensor receptors at the molecular level. Chemical sensors can be classified according to the type of active material as inorganic, polymeric or metal oxide. In biochemical sensors, a biochemical reaction occurs similar to chemical sensors [29].

In general, the main features that directly affect the operating efficiency of the gas sensor and that should be present in the sensor can be given as stability, selectivity, sensitivity, wide measurement range, resolution, operating temperature, response time, recovery time and sensor life [30]. However, depending on the conditions of use, it is not necessary for all of these features to be present in the sensor at the same time. The decisive factor here is the usage area and usage conditions of the sensor. For example, sensors used in the healthcare field are generally expected to have low concentration sensitivity at room temperature, while industrial sensors in high temperature environments do not need to operate at low temperatures. In detail, the features that are taken into consideration in the sensors are that they have high discrimination power, long life, easily portable, have a fast gas response and short regeneration time, and are low-cost and suitable for different operating temperatures [31].

When selecting or designing a sensor depending on the usage conditions, it is necessary to pay attention to the sensor types as well as their basic features. We can

basically categorize gas sensors into the following six groups according to their detection mechanisms [32];

- Optical gas sensors
- Acoustic-based gas sensors
- Capacitance-based gas sensors
- Calorimetric gas sensors
- Electrochemical gas sensors
- Metal oxide semiconductor gas sensors

## 1.4 Metal Oxide Semiconductor Gas Sensors

The performance of gas sensors is directly affected by the components of the sensor mechanism. Researchers who are aware of this situation continue to work on areas such as the sensor's substrate, sensing surface type, sensing surface morphology and integration of the sensing surface onto the substrate. In recent years, metal oxide semiconductor materials have been used as sensing surfaces in gas sensors to improve their performance. Various applications and general characteristics of metal oxide semiconductor gas sensors are shown in Fig. 1.8. In this type of sensor, metal oxide semiconductor materials are deposited on the substrate and contact of this surface with the target gas is ensured. Changes on the sensor as a result of the interaction between the metal oxide semiconductor surface and the target gas provide measurement information.

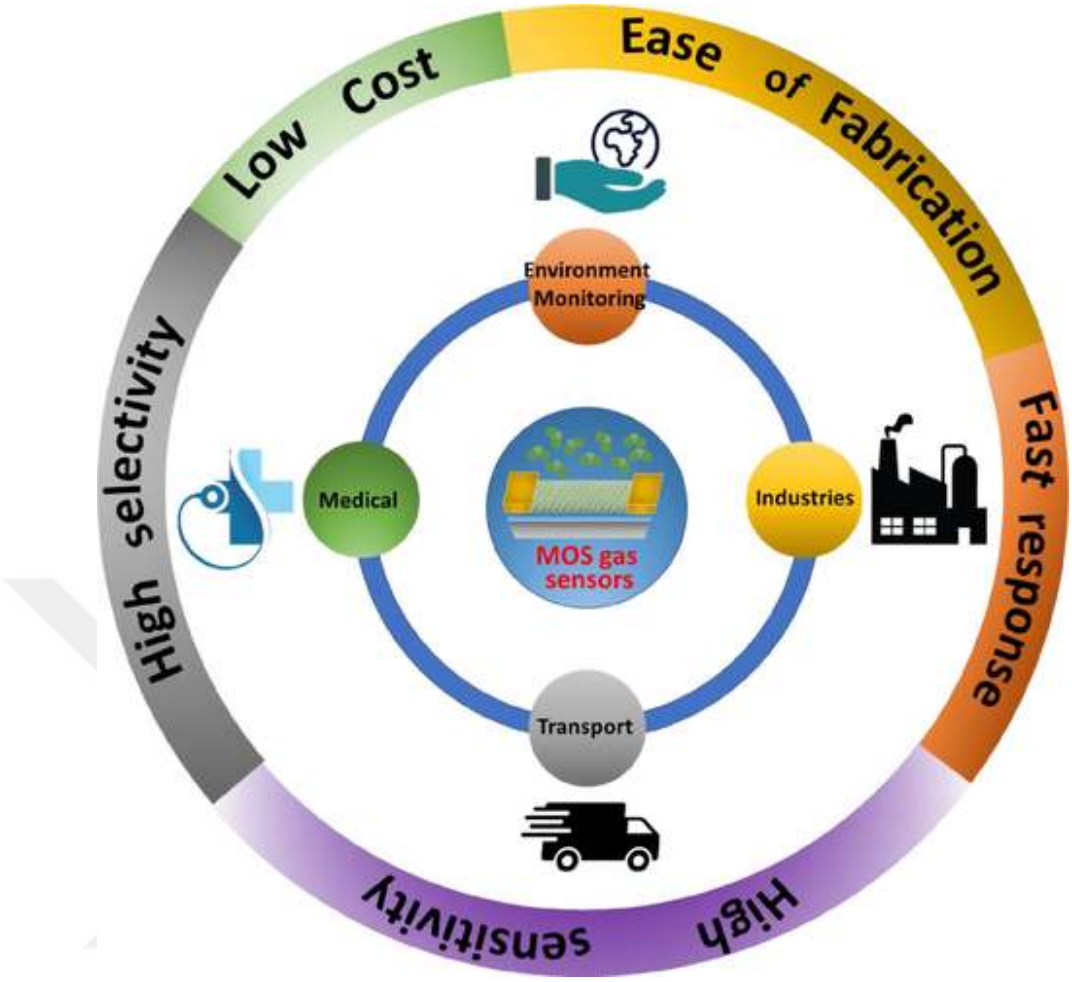


**Figure 1.8.** Applications and general characteristics of metal oxide semiconductor gas sensors [30].

The basis of the gas measurement mechanism in MOS sensors is based on electrical resistance change. When the sensor surface comes into contact with the target gas, an electrical resistance change occurs. In fact, this situation begins when the semiconductor comes into contact with air and retains oxygen, increasing the electrical resistance. Free electrons on the semiconductor surface bond with oxygen atoms and electrical conductivity decreases. The free electrons bound by oxygen then increase or decrease the electrical conductivity depending on the type of gas and metal oxide when contact with the target gas occurs. Thanks to this change in the electrical resistance, the reading is made on the gas sensors [33].

MOS gas sensors are more reliable than other gas sensors due to their sensitive chemical mechanisms at different pressures and temperatures, and as the temperature increases, the detection performance of the sensor increases up to a certain point [34].

### 1.4.1 Gas Sensing Mechanism of Metal Oxide Semiconductor Gas Sensors

MOS gas sensors can be considered in the group of electrically based chemical sensors. The two most important parts of the gas detection mechanism of MOS gas sensors are the target gas sensing surface and the transducer unit, where there are many receptors. Receptors are the part of the sensor unit that interacts physically or chemically with the target gas during target gas adsorption or desorption. The transducer unit is the part that enables the physical processes occurring during this interaction process to be converted into electrical and optical etc. signals. Surface oxygen of metal oxides play a very important role in gas sensing. A change in receptors can cause significant changes in sensitivity [35]. In addition to oxygen, water molecules and hydroxyl groups in the environment are also adsorbed by the metal oxide semiconductor surface. However, due to oxygen's high affinity for electrons, oxygen ions play the most important role in the detection mechanism [36].

Oxygen adsorption onto the sensing material can occur as either $O_2^-$ in molecular form or $O^-$ or $O^{-2}$ in atomic form, depending on the temperature of the environment. Oxygen ions on the metal-oxide surface are very active against the target gas. In general, $O^{-2}$ ions are adsorbed at temperatures below 147°C, while $O^-$ ions are adsorbed at temperatures between 147 °C and 397 °C. $O_2^-$ ions are ions adsorbed at temperatures of 397°C and above. Oxygen species adsorbed by the surface cause significant changes in the electrical conductivity of the sensing material. This change may occur in the form of an increase or decrease depending on the type of semiconductor that is the sensing material (depending on whether it exhibits n-type or p-type behaviour) [37].

#### *1.4.1.1 Gas Sensing Mechanisms of N-Type and P-Type Metal Oxide Semiconductors*

Depending on the temperature, oxygen accumulates on the surface of the N-type semiconductor (mostly charge carriers are electrons) under atmospheric conditions. Electrons are transferred from the semiconductor sensor towards the oxygen on the surface. Due to the decrease in electron density, an electron depletion layer forms on the MOS surface. For this reason, a potential barrier forms on the particle surface. This causes an increase in sensor resistance. When the sensor in this state is exposed to a reducing gas, an interaction occurs between the reducing gas and the oxygen on the surface. The electrons released as a result of this interaction return to the depletion layer. This process causes the electron depletion layer to decrease and the potential barrier energy to decrease. Thus, the resistance of the sensor decreases. If this sensor is exposed to an oxidizing gas, it will, on the contrary, take electrons from the conduction band, causing the resistance of the material to increase [38].

Due to the oxygen species accumulated on the surface of the P-type semiconductor metal oxide sensor unit, electrons on the surface of the sensing unit move towards these oxygen. As a result, the hole concentration in the P-type semiconductor increases. This causes an increase in the conductivity (decrease in resistance) of the semiconductor. In the P-type semiconductor, which is exposed to reducing gas with oxygen accumulated on its surface, the oxygen interact with the target gas and release electrons into the environment. These electrons go to the conduction band of the material (decreasing the hole concentration) and causing the resistance to increase. If the target gas is an oxidizing gas, it will complete the process by taking electrons from the conduction band. In this case, the electrical resistance of the sensor material will decrease [39].

As a result, in N-type semiconductor metal oxide sensors, if the target gas is a reducing gas, the conductivity increases, and if the target gas is an oxidizing gas, the conductivity decreases. If the semiconductor exhibits P-type behaviour and is exposed to a reducing gas, the conductivity will decrease, and if it is exposed to an oxidizing gas, the electrical conductivity will increase.

### 1.4.2 Factors Affecting Gas Detection Parameters

#### *1.4.2.1 Temperature*

Detection of the target gas in gas sensors depends on the adsorption kinetics of the target gas in the sensing layer. The highest sensitivity in gas sensors occurs when adsorption and desorption rates are in balance at the optimum operating temperature. When studies in the literature are examined, it is known that MOS gas sensors are much more sensitive and respond faster at high temperatures (200°C – 500°C) [36] [40]. Organic materials, unlike metal oxides, can operate efficiently at temperatures below 200°C as well as at room temperatures [41]. In both metal oxide-based and organic-based gas sensors, the optimum operating temperature is determined mostly by trial-and-error method.

Li et al. operated at various temperatures between 25°C and 300°C using the $In_2O_3$ nano cubes they created as detecting units for Ammonia ($NH_3$), Nitrogen dioxide ($NO_2$), Carbon monoxide (CO), Hydrogen sulphide ($H_2S$), and ethanol gases. The greatest sensitivity was determined against $H_2S$ gas at 25°C, whereas the highest sensitivity was obtained against $NO_2$ gas at 100°C, according to temperature-dependent studies [42]. Bian et al. investigated the ammonia gas sensing capabilities of ZnO nanoparticles produced via electrospinning. Their investigation led them to the conclusion that 340°C was the temperature at which the sensor had the shortest reaction and return times [43]. Altındal et al. synthesized phthalocyanine in a spherical structure to examine the carbon dioxide ($CO_2$) detection performance and determined the optimum operating temperature as 127$^oC$ with a concentration of 200 ppm [44].

Another factor affecting the optimum operating temperature is the doping process applied to the gas sensing surface. Zainab et al. produced polyaniline nanofibers by hydrothermal method using different solvents. They tested the thin film sensors produced for hydrogen sulfide gas detection at 150$^oC$, 100$^oC$ and room temperature. In the study where the effect of solvent and operating temperature was examined, efficient results were obtained for all solvents at room temperature [45]. Liu et al. examined the effect of tungsten doping on the performance of titanium dioxide in butane gas detection. When 7.5% tungsten was doped to the titanium dioxide sensing

surface, the optimum operating temperature was 440°C, while the best performance was observed at 420°C with 5% Tungsten (W) doping [46].

#### *1.4.2.2 Humidity*

One of the important factors affecting the operating performance of gas sensors is the amount of humidity in the environment. As it is known, there is a mechanism basically based on adsorption-desorption steps on the sensor gas sensing surface. As the amount of humidity in the environment is high, the areas required for oxygen ionization before the gas detection step are restricted. There is a decrease in the active sites where oxygen can bind and receive electrons. Additionally, humidity in the environment may show a reducing gas behaviour. This may cause electron transfer to the gas sensing surface, causing a change in the gas sensing surface resistance even though the target gas does not enter the environment [36] [40].

Itoh et al. examined the sensitivity of the $WO_3$ sensing surface to toluene gas at 400°C by changing the humidity of the environment at 25%, 50% and 75%. According to the results of the research, it was observed that as the humidity in the environment increased, there was a significant decrease in sensor sensitivity [47]. Fomekong et al. produced ZnO gas sensors by spray chemical vapor deposition method and examined their sensitivity to CO, $NO_2$, and NO gases. When the humidity rate increased from 2.5% to 10%, the selectivity rate in the ZnO gas sensor increased against $NO_2$/CO gases, but the recovery time for $NO_2$ gas decreased significantly. They explained the reason for this as water molecules adhering to the gas sensing surface and a decrease in the adsorption of $NO_2$ gas [48]. Cho et al. increased the humidity rate by 0%, 5%, 10%, 15% and 20% in the measurements of the polypyrole gas sensor they produced for methanol detection. When the sensor sensitivity results were examined, it was observed that the highest sensitivity was in a moisture-free environment [49]. Cheng et al. produced a ZnO thin film gas sensor using the radio frequency scattering method to measure the hydrogen gas sensing properties. During the measurement, the humidity in the environment was increased and the sensor sensitivity decreased by up to 70%. In measurements made at 250°C, no response was received from the sensor after 70% humidity. According to this study, as the amount of humidity increased, water

molecules accumulated on the sensor sensing surface and gas detection could not occur after a specific point [50].

#### *1.4.2.3 Doping with Different Elements*

Doping the sensing surface of MOS gas sensors with different elements can increase the sensing efficiency of the sensor. Grain size change, surface roughness and defects on the sensing surface with doping affect the parameters of the sensor such as sensitivity, response and recovery time. While proportional doping positively affects sensor performance up to the optimum level, it has a negative effect after a certain amount [51].

Lyson et al. investigated the effect of chromium (Cr) doping on a hydrogen gas sensor with a $TiO_2$ sensing surface. The $TiO_2$ surface, to which 0.5, 1, 5 and 10% Cr was added by mass, exhibited the highest sensitivity with 5% Cr contribution in measurements performed at 250$^oC$. For this study and temperature, 5% Cr contribution shows the optimum doping value [52]. As can be seen, the doping rate specifically reduces sensor performance after reaching the most efficient point. In another study, Khudiar et al. produced $SnO_2$-based hydrogen gas sensors and examined the effect of Al doping. The doping rate in the study varied between 1 and 3.5%. The sensor response increases proportionally until the doping rate reaches 3%. It has also been observed that sensors with this doping rate are the fastest responding sensors. When the Al doping rate exceeds 3%, sensor performance was decreased [53]. Zeng et al. studied the effect of niobium doping on $TiO_2$-based gas sensor. They exposed the $TiO_2$ sensing surface produced by the hydrothermal method to acetone, ethanol, methanol and formaldehyde gases by doping it with Niobium (Nb). When they analyzed the detection properties, they observed an increase in the sensitivity of the Nb-doped $TiO_2$ sensor. They also reported a significant reduction in response and recovery time [54]. In their study examining the sensitivity of the ZnO gas sensor to $NH_3$ gas, Nakarungsee et al. proved that doping plays an important role on morphology of nanostructures. They noticed that the morphology of ZnO is transformed from block-shape into thin flake- shape by doping ZnO with 1 and 3% Cr dopant, in which the mixture of nanorods and nanostructures appear. Nevertheless, higher doping rates cause relatively smaller particles, resulting in a rougher surface [55].

#### *1.4.2.4 Morphology and Surface Properties*

In gas sensors, the morphological structure of the sensing surface and its nano or micro dimensions directly affect the operating parameters of the sensor. Depending on the changing morphology and particle size, the amount of oxygen that can adhere to the sensing surface and therefore the resistance change mechanism of the sensor varies. The reason for this is the formation of different numbers of active sites in different morphologies and surface areas. The morphology of the sensing surface varies depending on parameters such as production method, process time, solution concentration, temperature, pH and pre-treatments before production [56] [40].

Zhang et al. examined the effect of particle sizes on sensor performance in the $In_2O_3$-based gas sensor they produced for ethanol gas detection. At the end of the study, as the particle size decreased, the detection surface area in contact with the target gas increased and therefore the sensor sensitivity increased [57]. In another study, Lee et al. investigated the sensitivity of the sensor to $NO_2$ gas by producing a Copper (Cu) phthalocyanine-based gas sensor on substrates at different temperatures (28, 100, 150 and 200°C). While an agglomerated morphology was observed on the sensing surface at initial temperatures, as the temperature increased, the morphology turned into a fiber-like structure. However, the most efficient detection results were achieved at 100°C [58]. This study clearly shows that the sensing surface morphology changes depending on temperature. To examine it more deeply, increasing the gas detection surface area with morphology change improves the sensor performance. Han et al. produced a $SnO_2$-based gas sensor to examine CO gas detection parameters. In the study, they used thermal evaporation as a thin film production method and examined the relationship between sensitivity and particle size on the detection surface. As a result, the sensor with the highest sensitivity was determined to be the sensor with the lowest particle size on the sensing surface. As the particle size on the surface decreased, the amount of oxygen adsorption-desorption and the area in contact with the target gas increased [59]. Banimuslem et al. investigated the effect of surface roughness as well as particle size on sensor sensitivity. In their study where they measured $NH_3$ gas, the gas detection surface was a thin film of fluorinated chromium phthalocyanine annealed at 100, 300 and 400°C. According to the results of surface

roughness measurement by atomic force microscope (AFM), roughness decreased as the annealing temperature increased. As a result, the highest sensor sensitivity was observed on the sensing surface annealed at 100°C [60]. One of the factors affecting morphology change and therefore sensor performance is solution pH change during the production process. Very significant changes in morphology occur with pH change. Singh et al. examined the effect of pH change on morphology in the production of ZnO nanostructures. The nanorod structure formed when the pH value was 8 turned into nanoparticles as the pH value increased. The performance of sensors with nanorod and nanoparticle sensing surfaces was observed by exposing them to equal amounts of propanol, ethanol and methanol gases at 400°C. It was reported that the sensitivities of the sensors, which initially responded to all three gases, changed as the pH increased and thus the sensing surface increased with the transformation from nanorod to nanoparticles [61].

### 1.4.3 Performance Parameters of Gas Sensors

#### *1.4.3.1 Optimal Working Temperature*

Due to the working mechanism of gas sensors, it is vital for the sensors to react with the target gas and provide the ideal sensor response. This situation, which includes the step of adhesion of the target gas to the sensor surface, is directly related to the temperature of the environment. Temperatures at which optimum performance can be achieved may vary for each sensor. When looking at the literature, there are sensors that have their optimum properties above 500°C, while optimum operating temperatures are generally specified between 100 and 500°C. In addition, there are sensors that provide optimum operating conditions at room temperature [62] [63].

#### *1.4.3.2 Limit of Detection*

One of the most important features that determine the performance parameters of gas sensors is their ability to detect the target gas in concentrations as low as possible. The detection limit is the minimum concentration of a target gas that a gas sensor can detect under certain conditions [62].

#### *1.4.3.3 Sensitivity*

The maximum change between the start signals before the gas sensor sensing surface interacts with the target gas and the end signal after it interacts is expressed as sensitivity. These signals may be physical parameters such as resistance, conductivity, photoluminescence, and the detection limits of the sensor can be determined with these parameters [64].

#### *1.4.3.4 Stability*

An ideal gas sensor should be able to maintain its initial performance within a certain operating range after performing for a long time. This feature can be described as stability for the gas sensor. If the sensing surface cannot maintain its stability, the working life of the sensor is shortened and frequent sensor replacement is required in the application area. Therefore, it is very important that gas sensors maintain their long-term stability in practical applications The main factors affecting the stability of gas sensors are operating temperature, type of sensing or substrate material, humidity level and corrosiveness of the environment [29].

#### *1.4.3.5 Selectivity*

The detection surface of gas sensors can show the same reactions to the target gas and non-target gases in environments where many gases are chemically very similar. This situation causes serious problems in application areas. For this reason, an ideal gas sensor is expected to detect and react to the target gas among various gases in the environment. Therefore, selectivity is one of the most important parameters among the gas sensor performance parameters and is a parameter that indicates that the target gas can be easily detected even if there are different gases in the environment [35] [65].

#### *1.4.3.6 Response and Recovery Time*

When the sensor surface of gas sensors interacts with the target gas, it takes a certain period of time for them to show maximum response. The saturation point of each gas sensor in detecting the target gas may differ. This time is defined as the response time and is the time from the initial signal to the 90% level of the final signal value after

the sensor is exposed to the target gas. The time it takes for the sensor to reach its initial value when the target gas leaves the environment after reaching its maximum detection value is called the recovery time. Unlike disposable sensors, gas sensors that will be used repeatedly must have this feature. Response and recovery times may vary depending on the temperature of the environment in which the gas sensor is used, the morphological structure and type of the sensor surface, and the concentration of target gas molecules [66].

## 1.5 ZnO Coating Methods

### 1.5.1 Hydrothermal Method

Various processes can be utilized to manufacture ZnO functionalized textile substrates. Hydrothermal synthesis is a method of obtaining different types of materials and compounds depending on the desired size and morphology, based on the use of various physical and chemical processes occurring in aqueous solutions with temperature and pressure control [67]. Hydrothermal synthesis offers several key benefits, including highly variable reaction kinetics based on temperature, the ability to produce single crystals, the capability to generate high-purity products from initially impure raw materials, cost-effectiveness, and environmental friendliness [68]. Moreover, the hydrothermal method allows precise control over the morphology and size of the film by adjusting parameters such as temperature, pressure, pH, and the composition of the starting solution during the powder synthesis process. Krsovska and colleagues obtained ZnO in nine different morphologies on the glass plates by changing the concentration, seeding methods, growth time and temperature of the reagents, and the pH of the starting solution in the hydrothermal synthesis process [67]. Akçakoca et al. investigated the impact of the pH (ranging from 2 to 15) and synthesis time (ranging from 30 minutes to 24 hours) on nanopowder production by hydrothermal synthesis [69].

Based on the ongoing studies, fundamental parameters like solution concentration, reaction temperature, and duration can directly influence the outcomes. The seed layer process is another critical step that significantly impacts the results. Factors such as the type of the process, duration, temperature, and composition of the seed layer play

crucial roles in hydrothermal coating studies. One of the important variables that directly affects coating quality is the seeding process [70]. Basavaraj et al. investigated the annealing effect of ZnO seed layer in ZnO nanorod growth. ZnO nanorods deposited on the annealed seed layer exhibited vertical alignment, and showed higher aspect ratio and higher peak intensity in X-Ray Diffraction (XRD) characterization [71]. In another research made by Su and colleagues, investigation of the effect of seed solution concentration on the morphological, structural and optical properties of ZnO nanorods produced by hydrothermal method was carried out. An increase in solution concentration led to larger and more uniform diameters of ZnO nanorods, resulting in improved crystal quality. Additionally, nanorods on the surface became denser and exhibited a more homogeneous structure [72]. Zhu et al. investigated the effect of ZnO seed layer thickness on nanorods produced by the hydrothermal method. At the nanorods grown on polydimethylsiloxane substrate, the average length, diameter and density increased with the increase in seed layer thickness from 20 to 60 nm, and decreased when the thickness increased from 60 to 80 nm. The aspect ratio, however, increased continuously when the seed layer thickness increased from 20 to 80 nm [73]. Overall, studies indicate that the seed layer process plays a critical role in metal-oxide coatings produced by using the hydrothermal method. Particularly, when applying metal oxides to fabrics through this technique, the seed layer significantly impacts properties such as coating homogeneity, morphology, crystal structure, uniformity, diameter, and length of the structures.

## 1.6 $NH_3$ Gas Sensors

$NH_3$ is a colorless gas with a strong odor with its primary source as nitrogen-based fertilizers used in agriculture. Other contributors to $NH_3$ emissions typically include the transportation industry, pharmaceuticals, and the production of cleaning products [74] [75]. $NH_3$ is an important hydrogen source that can be used to reduce the harmful effects of $NO_x$ gases [75] . Besides this beneficial feature, it can cause serious harm to human and living life. Especially when exposed to $NH_3$ above a certain threshold value, it can cause irritable effects on the eyes, skin and respiratory system. When inhaled, this gas destroys the soft membranes of the respiratory tract and lungs, causing a burning sensation, headache and shortness of breath, while extended exposure to this

gas can lead to fatalities. The environmental and health organizations of various countries have established threshold values for $NH_3$ in hazardous chemical substance regulations. As a general acceptance, $NH_3$ concentration in working environments should not exceed 50 ppm [76] [77]. For this reason, it is vital to systematically measure and monitor $NH_3$ in a controlled manner to prevent excessive exposure to the gas and mitigate potentially fatal outcomes.

## 1.7 Kevlar Fabric Substrate

Poly (p-phenylene terephthamide) (PPTA) fiber is a type of high-performance fiber that is also known by several brand names such as Kevlar™, Twaron™ and Armos™. It is widely recognized as one of the top three high-performance fibers globally [78]. Kevlar™ is a synthetic organic material produced by the condensation reaction of an acid chloride (terephthaloyl chloride) and amine (1,4 phenylene-diamine) (Fig. 1.9a), studies of which began in 1965. Kevlar™, which consists entirely of aromatic polyamides (aramids), stands out with its long and well-directed intermolecular chain structure, chemical composition, and similar properties to other synthetic fibers (Fig. 1.9b). Kevlar™ has many notable advantages including exceptional traction resistance, high impact resistance, remarkable chemical resistance to acids and bases (excluding concentrated forms), outstanding abrasion resistance, commendable fire resistance with self-extinguishing capabilities, low specific mass, limited electrical conductivity, and excellent performance under high temperatures. Because of the para-orientation of the benzene rings, Kevlar™ chains generally tend to form a planar sheet and are relatively rigid. In this way, when a strong physical impact is applied to Kevlar™ from outside, the H bonds lock the chains together and form a layer with very high tensile strength. Given its exceptional characteristics, Kevlar™ is utilized in a wide array of applications, including but not limited to tires, brakes, clutch linings, composite materials for strengthening, racing sails, bullet-proof vests and body armor, as well as in the aerospace and aviation sectors.

Kevlar™ has some weaknesses as well including challenging processing, absorption of moisture, and comparatively low compressive resistance. The smooth surface of the highly amorphous skin of the Kevlar™ fibers is due to random distribution of Kevlar™

molecular chains in the skin area, which brings with it the difficulties of coating and matrix adhesion [79] [80]. The low surface free energy and chemical inertness of Kevlar™ cause its poor adhesion which negatively affects the functionality and durability of the structure of the composites [81] [82]. Several strategies are employed to produce functional groups that enhance the interaction with the polymer matrix. Various surface treatment techniques are utilized in literature, such as ultrasonic treatment, heat treatment, γ-ray irradiation, plasma modification, etching, cryogenic treatment, and chemical treatment, to tackle challenges and bolster interfacial adhesion strength [80] [83] [84] [85] [86] [87]. It is well known that the effects of plasma physical etching and chemical modification decline with storage time extending, namely aging. The improvements of surface properties do not decay with time [88]. For these reasons, improvements or treatments that cause surface properties are valuable findings of critical importance.

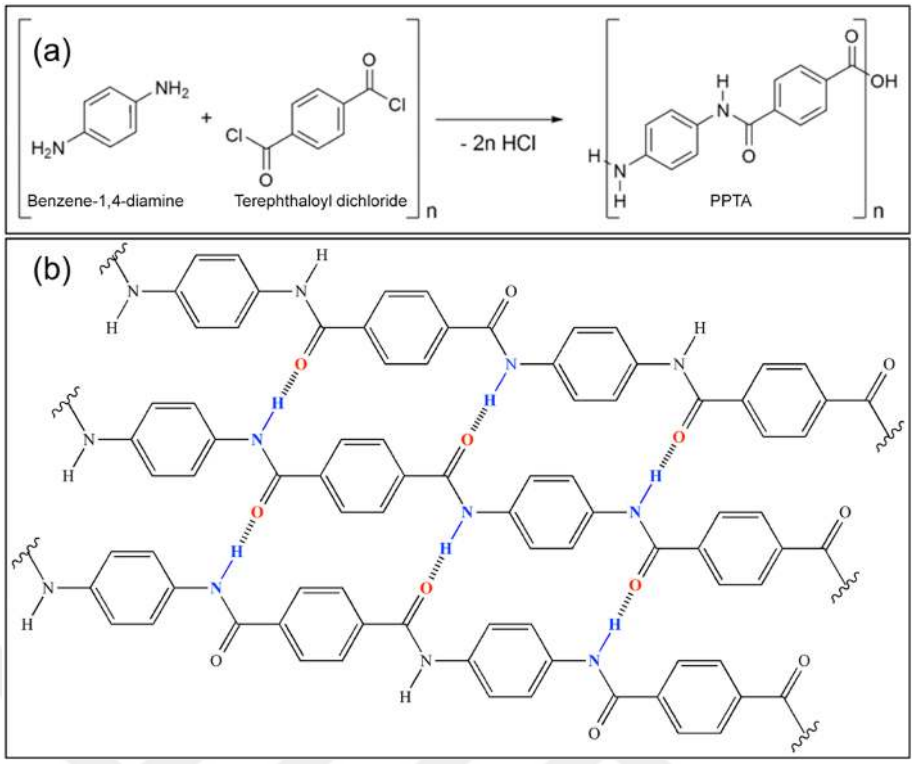


**Figure 1.9** a) The reaction of benzene 1,4- diamine with terephthaloyl chloride yielding PPTA, b) The PPTA structure consisting of the arrangement of hydrogen-bonded sheets in a radial stacking configuration.

Considering all these factors, in this study, Kevlar™ fabric was chosen as the substrate due to its flexibility and high thermal resistance. This study aims to investigate the impact of different seed layer processing times on the morphology of ZnO under constant hydrothermal coating conditions. Additionally, it seeks to examine how these different morphologies, when applied on a Kevlar™ fabric substrate, influence the sensor's sensitivity and selectivity to $NH_3$ gas. ZnO growth on the fabric was achieved using the hydrothermal method, with varying durations of ultrasonic bath seeding processes. Throughout the hydrothermal process, temperature, time, and solution contents remained constant. According to the literature research, this study is pioneering as it introduces and employs seeding with the ultrasonic method and investigates the influence of seeding duration on morphology. Furthermore, it stands out as the first known research to produce an $NH_3$ gas sensor using a ZnO coating with 1D-2D morphology on Kevlar™ fabric, providing insights into its performance.

# CHAPTER 2

## EXPERIMENTAL PROCEDURE

### 2.1 Coating Process of Kevlar Fabrics

200 g/m$^2$ plain water repellent ballistic Kevlar™ fabric with dimensions of 24 x 24 mm was used as substrate for the coatings. Zinc acetate dihydrate ($(CH_3COO)_2Zn \cdot 2H_2O$) (Sigma Aldrich), sodium hydroxide (NaOH), and ethanol were used for the seed solution. The hydrothermal synthesis coating process was performed in 60 ml steel pressure-resistant autoclaves. This involved preparing a solution comprising zinc nitrate hexahydrate ($Zn(NO_3)_2.6H_2O$) (Alfa Aesar), hexamethylenetetramine ($C_6H_{12}N_4$) (Sigma Aldrich), polyethyleneimine (PEI), ammonium hydroxide, and deionized (DI) water.


**Figure 2.1** Kevlar™ fabric surface treatment steps.

Before the seeding process, the Kevlar™ fabrics underwent a series of preparation steps. Initially, they were immersed in acetone (AE) for 10 min at 55°C within a closed system. After drying for 15 min, they were placed in ethanol (EtOH) for 10 min at 75°C and subsequently dried at 40°C for 30 min. Kevlar™ fabric surface treatment steps are shown in Fig. 2.1. Following this preparation, a solution was prepared by mixing 0.0125 M zinc acetate dihydrate and 0.02 M NaOH in 100 ml of ethanol at 65 °C for 45 min using a magnetic stirrer. The resulting solution was then transferred to an ultrasonic bath device, where the cleaned Kevlar™ fabrics underwent seeding using the ultrasonic bath method for durations of 1, 2.5, 5, 10, and 20 minutes. Kevlar™ fabrics seeding process steps are shown in Fig. 2.2. The seeded materials are expressed

as N1 (1 min), N2.5 (2.5 min), N5 (5 min), N10 (10 min) and N20 (20 min) depending on their duration time throughout the process.

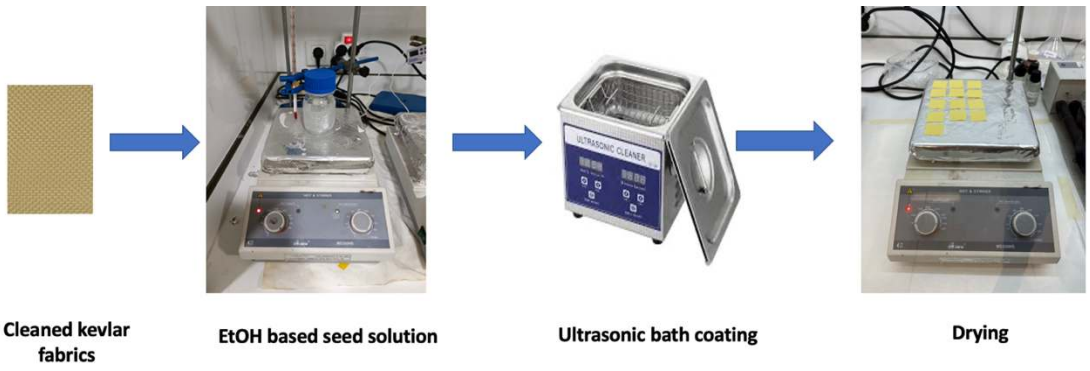


**Figure 2.2** Kevlar™ fabric seeding process steps.


**Figure 2.3** Steps of coating Kevlar™ fabrics by the hydrothermal method.

For the hydrothermal coating process, a solution was prepared using the following concentrations: 0.048 M zinc nitrate hexahydrate, 0.024 M hexamethylenetetramine, 0.0077 M polyethyleneimine, 0.49 M sodium hydroxide, and 100 ml of DI water. The solution was stirred at room temperature for 60 min using a magnetic stirrer. Next, the fabrics were immersed in the solution, which was then transferred to 60 ml autoclaves in 30 ml volumes. The hydrothermal coating process was conducted at 85°C for 5 h. Following the completion of the process, the coated fabrics were rinsed with DI water and subsequently annealed at 100°C for 1 h. The steps of coating Kevlar™ fabrics by the hydrothermal method are shown in Fig. 2.3. For electrical measurements, interdigital transducer (IDT) electrodes were created with a defined geometry by manually applying highly pure (>99.99%) silver paste onto the coated fabrics. The ZnO nanorods on fabrics seeded for 1 and 2.5 min appear sparse and in

inhomogeneously distributed on the surface. Therefore, it was decided to use and produce N5, N10 and N20 sensors on Kevlar™ fabrics.

## 2.2 Material Characterizations and Gas-Sensing Measurement System

The crystal structure of Kevlar™ was characterized by a Rigaku Miniflex 600 Tabletop X-Ray diffractometer with a $CuK_{\alpha}$ radiation scanning between 20 and 50˚. Raman spectra were recorded by using an NRS-4500 Series Confocal Raman Microscope with a laser wavelength of 532 nm. The laser power at the sample was about 4.5 mW. Spectra shown in this work were recorded at 1 $cm^{-1}$ step. All the spectra are presented without any further manipulation. The Fourier transforms infrared spectra (FT-IR) of Kevlar™ were recorded on a FT/IR-6X Spectrometer (Japan Spectroscopic Corporation, Japan) in the range of 3500-350 $cm^{-1}$. Finally, the effect of AE and EtOH on surface cleaning was examined with a Hitachi SU5000 scanning electron microscope (SEM).

The results of seeding and hydrothermal coating on Kevlar™ fabric substrate were analyzed using SEM with a Hitachi SU5000 instrument. In addition, the mass percentage of metal oxide and other materials on the fabric surface was determined through energy dispersive X-ray spectroscopy (EDS) examination. The crystallinity of both the seed layer and the rods was assessed by using the X-ray diffraction (XRD) method with a Rigaku Rint MiniFlex instrument.

Gas-sensing experiments utilized a local computer-controlled system equipped with temperature and humidity sensors, gas flow regulators, a Keithley 2400 current-voltage sourcemeter. The flow of gas onto sensors was managed by Alicat mass flow controllers (MFCs), with one controlling dry air flow (with a range up to 500 SCCM) and the other managing target gas flow (with a range up to 5 SCCM). A LabVIEW-based program controlled these devices to achieve desired gas concentrations. A cryogenic temperature controller (SRS-CTC100) maintained sensor temperature for accuracy. A protective sensor cell housed the gas sensor, shielding it from damage and contamination. Data acquisition, facilitated by a standalone Keithley 2400-unit, transmitted sensor data to a computer via GPIB card. Measurements were conducted

at a 3 V bias voltage and temperatures ranging from 25°C (RT) to 205°C, with a 5-min stabilization period at each temperature. Indoor air relative humidity during measurements was approximately 35%. Gas sensor production and characterization steps are shown in Fig. 2.4.

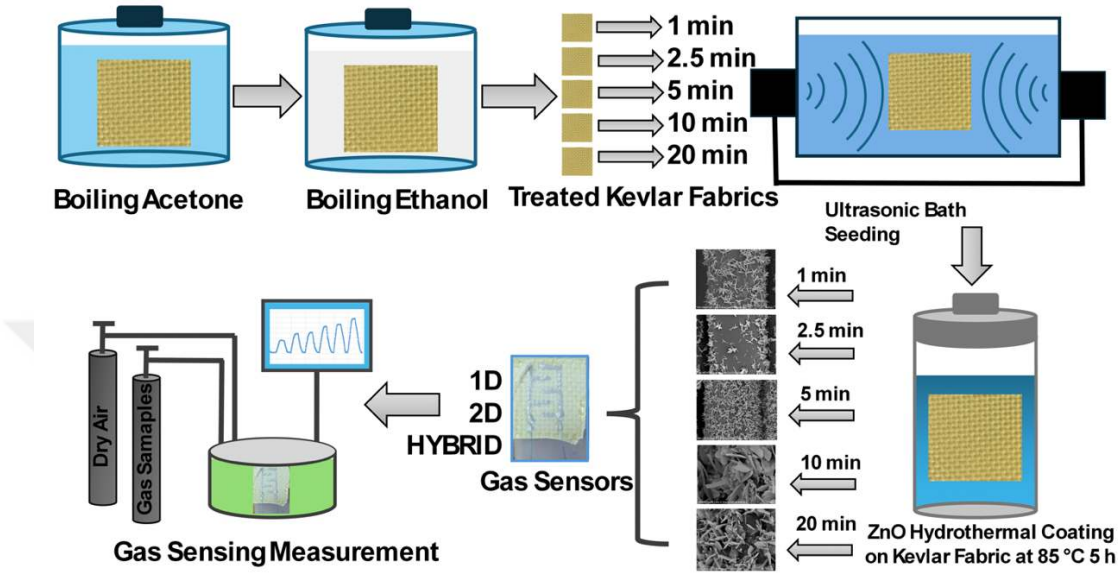


**Figure 2.4** Gas sensor production and characterization steps.

# CHAPTER 3

## RESULTS AND DISCUSSIONS

### 3.1 Kevlar™ Substrate Treatment

FT-IR spectroscopy is a useful method for comprehending the chemical and crystal structure of Kevlar™ fibers, examining how the polymer interacts with moisture it absorbs, assessing the impact of remaining impurities on the fiber's long-term performance, and evaluating and enhancing surface treatments to enhance adhesion. This study was an attempt to understand the structural disparities among the crystalline forms of Kevlar™ treated with AE and EtOH, as well as the untreated Kevlar™. Effects of the treatment process was examined by FT-IR (Fig. 3.1).

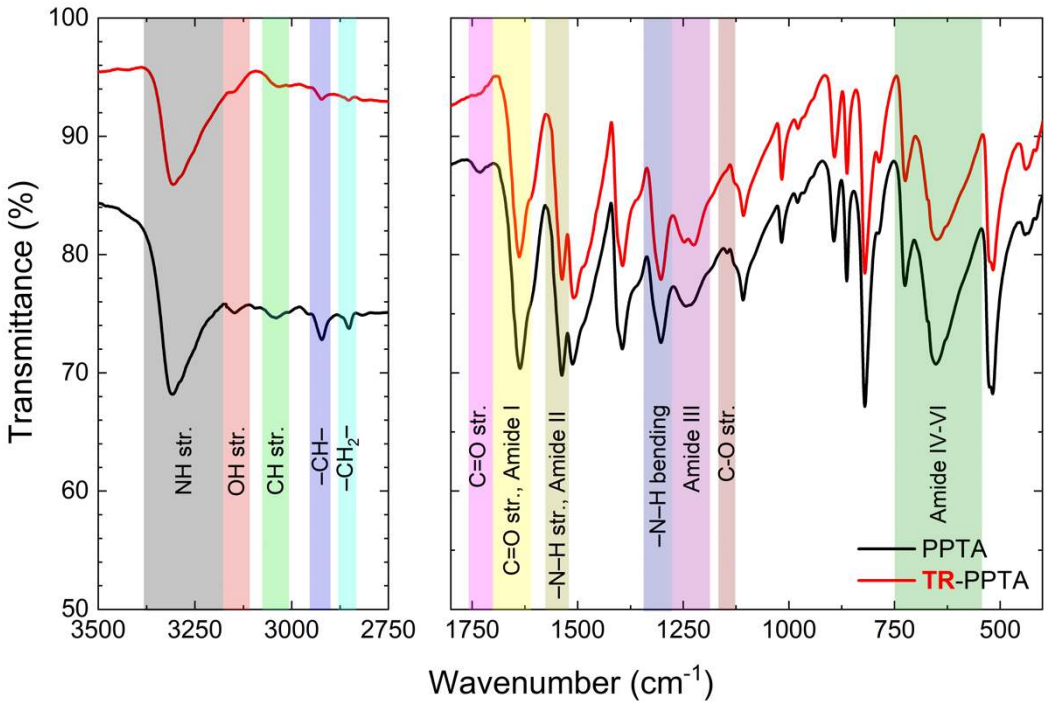


**Figure 3.1** FT-IR spectra of PPTA (Kevlar™) fiber before and after treatment.

The wide absorption peak observed at 3308 and 3307 $cm^{-1}$ in both Kevlar™ and TR-Kevlar™ can be attributed to the stretching vibration of N–H bonds. The peak

observed at 1637 and 1639 $cm^{-1}$ is a characteristic peak of amide I, specifically the stretching of C=O bonds. Similarly, the peak observed at 1538 and 1537 $cm^{-1}$ is a characteristic peak of amide II, which involves the coupling between N–H stretching and N–H bending vibrations. Lastly, the absorption peak observed at 1512 and 1510 $cm^{-1}$ can be attributed to the stretching of C=C bonds in the benzene ring. The obtained results agree with the published literature [89] [90] [91][92]. Compared to Kevlar™, the peaks corresponding to the stretching of –C=O and –C–O at 1732 and 1145 $cm^{-1}$ were disappeared in the TR- Kevlar™. These peaks are attributable to defects in the amine group that may be caused by chemical impurities, or the incorporation of chain ends into crystallites that disrupt the lateral packaging of molecules and/or their crystallites [89]. Furthermore, the peak observed in Kevlar™ at 1236 and 442/433 $cm^{-1}$ was found to be at 1226/1250 and 438 $cm^{-1}$ in the TR- Kevlar™, respectively. The observed peak correlates to the torsion and out-of-plane bending movements in the amine group. Ultimately, the procedure helps to improve the –C=O in the amine group and reduce the defects. Chatzi et al. reported that the AE and methanol treatment procedures were modified by replacing AE and/or methanol with water. Next analysis revealed that the hydrogen bonds oriented parallel to the surface of the film. They have previously attributed a peak at 883 $cm^{-1}$ to the hydrolysis of Kevlar™ at the surface of the fiber, which is caused by the production of carboxylate groups. This peak was observed during the process of boiling in sodium hydroxide solutions, which involved highly hydrolytic conditions [89]. Li et al. was reported that a new absorption peak appeared around 890 $cm^{-1}$, which shows that the oxidation of the C–H bond on the benzene ring, and the addition of oxygen-containing groups to the benzene [82]. Zhu et al. exposed Kevlar™ to $O_2$ plasma for various periods of time and observed a peak at 1218 $cm^{-1}$ that was unrelated to the Kevlar™ structure [82]. It was reported that this peak corresponds to the oxygen-containing stretching mode containing C- O group, which can be occurred by plasma treatment [82]. Kevlar™ fabrics were modified with acetic acid and silane. Acetic acid treatment of the fibers, C=O stretching band corresponding to 1718 $cm^{-1}$, and the peak of OH and CH stretching band that correspond to 2800-3000 $cm^{-1}$ has caused the emergence of broad cross-bands. In addition to acetic acid treatment of the fibers with silane treatment, the carbonyl stretching corresponding to 1718 $cm^{-1}$ showed the appearance of a new absorption

band, while the –NH groups depending on 3313 $cm^{-1}$ and 1538 $cm^{-1}$ peaks disappeared by virtue of the salination [91]. Ibrahim et al. observed a novel absorption peak at 3645 $cm^{-1}$ following the treatment of Kevlar™ fibers with phosphoric acid. This peak has been reported to be caused by the creation of hydroxyl groups, which are present in low concentrations and connected with aromatic rings [93]. The impact of various temperature and humidity levels on high-strength p-aramid fibers were investigated. However, the results showed only negligible alterations in these peaks, and no peaks associated with the synthesis of carboxylic acid were seen [92].

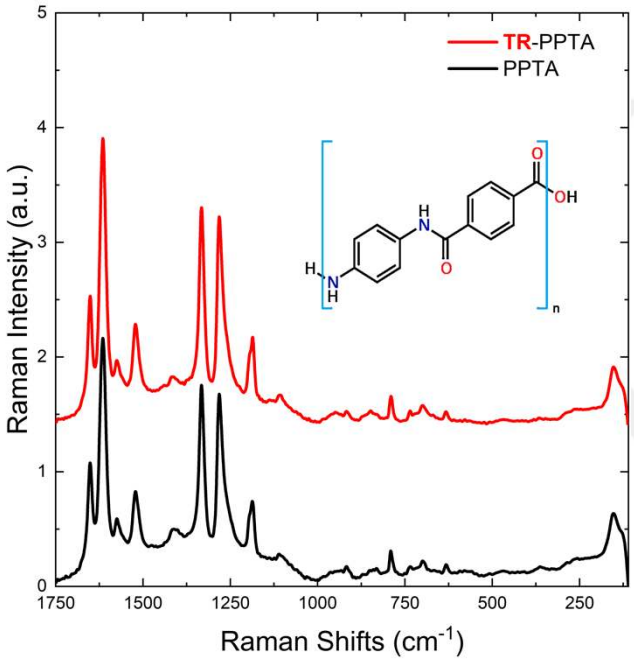


**Figure 3.2** Raman spectra of PPTA (Kevlar™) and TR-PPTA (TR- Kevlar™).

The Raman spectra of Kevlar™ fibers are displayed within the 100–1750 $cm^{-1}$ range for enhanced readability, as no spectral bands were recorded in the 1750–3000 $cm^{-1}$ region. The absence of bands in the 2900–3200 cm−1 area, which are typically associated with CH and NH stretching vibrations, was attributed to orientational effects. The spectra of Kevlar™ and TR- Kevlar™ (Fig. 3.2.) exhibit characteristic Raman bands at specific frequencies and in the following sentences, peaks of Raman spectra are given as untreated (Kevlar™) and treated (TR- Kevlar™), respectively. These include bands at 632 and 631 $cm^{-1}$, which correspond to the in-plane deformation of the CC ring. Additionally, bands at 698 and 699 $cm^{-1}$ indicate out-of-

plane deformation of the CH group and bending of the CO group. The bands at 733 and 735 $cm^{-1}$ represent in-plane bending of the CO group, asymmetric deformation of the CH group in the ring, and stretching of the CN group. Furthermore, bands at 846 and 849 $cm^{-1}$ signify out-of-plane deformation of the CH group, stretching of the ring CC bonds, bending and torsion of the ring, and 1184 and 1187 $cm^{-1}$ correspond to deformation of the CH group in the ring. The bands at 1280 and 1281 $cm^{-1}$ indicate bending of the NH group and stretching of the CN group. The bands at 1573 and 1574 $cm^{-1}$ represent vibrations of the amide II group, including bending of the NH group, stretching of the CN group, stretching of the ring CC bonds, and bending of the NH group. Lastly, the bands at 1613 and 1615 $cm^{-1}$ correspond to stretching of the aromatic ring CC bonds, and the bands at 1649 and 1651 $cm^{-1}$ indicate stretching of the CO group in the amide I group. The spectrum of Kevlar™ displays distinct Raman bands that are linked to p-substituted benzenes. These bands can be characterized by the prominent deformation bands at 789 $cm^{-1}$ and 1182 $cm^{-1}$, the NH bending and CN stretching band at 1280 $cm^{-1}$, and the intense band corresponding to the aromatic ring CC stretching at 1615 $cm^{-1}$ [94]. FT-IR and Raman analyses reveal that there is no evidence of any change in the molecular structure. In other words, the solvents (EtOH, AE) employed in the treatment did not form chemical bonds with the Kevlar™ molecules or cause the polymeric chains to fracture.

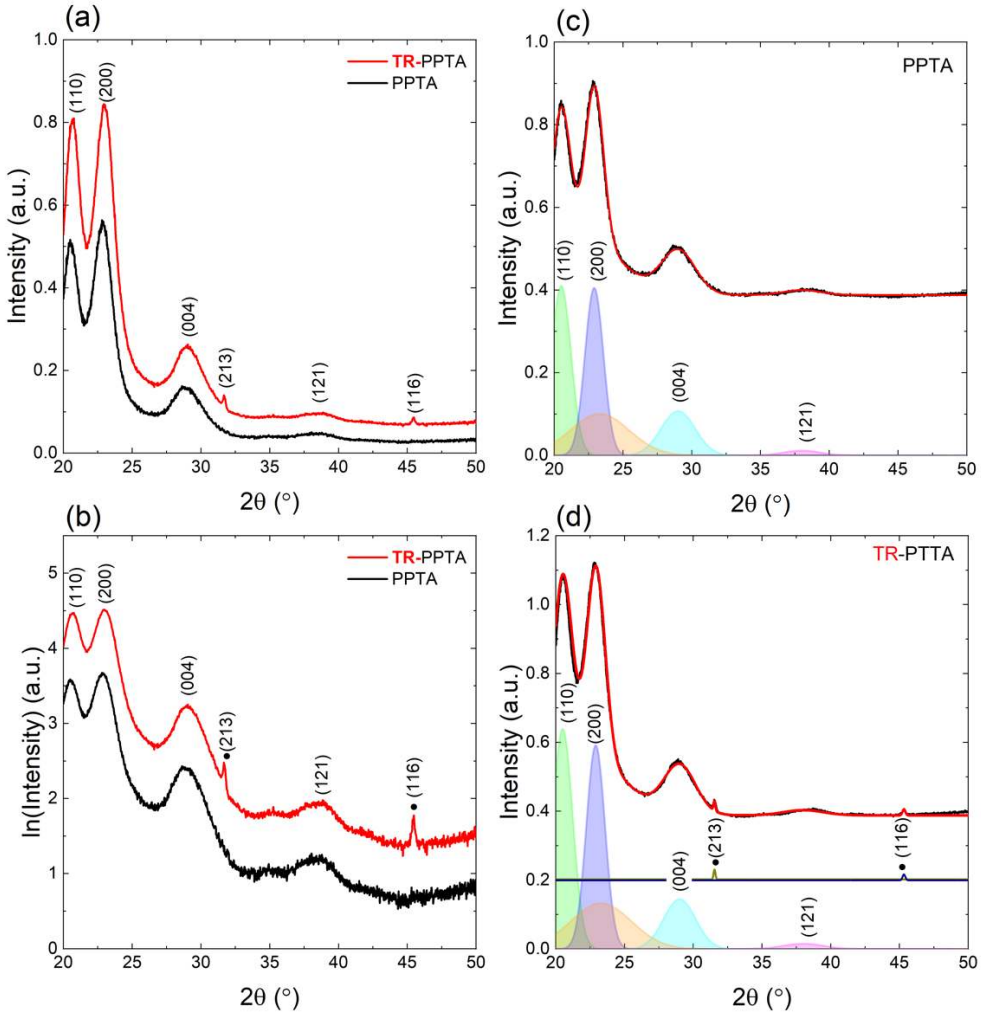


**Figure 3.3** a) XRD patterns of PPTA and TR-PPTA in a) linear, b) logarithmic scale of intensity versus 2θ, c) Gaussian fitting of XRD peaks for c) PPTA and, d) TR-PPTA fabrics.

Fig. 3.3 depicts the XRD patterns of Kevlar™ and TR- Kevlar™ in linear and logarithmic scale of intensity versus 2θ. The intent in using logarithmic scale is to know that it emphasizes low intensity peaks. The X-ray spectra of both fabrics have strong diffraction peaks at about 20.5, 23.0, 29.1 and 38.0° corresponding to the (110) and (200), (004) and (121) plane of Kevlar™, respectively [95] [96] [97]. The molecular structure of Kevlar™ fibers is monoclinic, resembling an orthorhombic structure. The dimensions of the unit cell are as follows: a = 7.87 Å, b = 5.18 Å, and c (fiber axis) = 12.9 Å [98]. The crystal structure of Kevlar™ fibers can be described as layer-like. The (200) plane primarily exhibits the effects of van der Waals forces and,

to a limited degree, π-electron overlap. The crystal plane (110) reflects the distance between adjacent polymer chains, which are described by a conspicuous concentration of non-bonded, intermolecular interactions. The crystallinity $X_c$ (%) of the aramid fiber was calculated from:

$$X_c(\%) = \left[ \frac{\sum A_c}{\sum (A_c + A_a)} \right] \times 100 \quad (3.1)$$

where, $A_c$ is the area under the peaks in the diffractogram and $A_a$ is the integration of the amorphous halo [99]. Peak areas of untreated and treated Kevlar™ fibers were presented in 3.3 b and d, respectively. Based on the Scherrer equation,

$$D = \frac{0.94\lambda}{\beta cos\theta} \quad (3.2)$$

where λ is the wavelength of X-ray source, β is the full width at half maximum (FWHM), θ is the Bragg angle and D is the size of crystallites. Given that neither of the peaks predicted a shift, the 2θs were fixed. In order to assess the impact of the treatment process on the structure and crystallinity of Kevlar™, the XRD pattern of both specimens was recorded and presented in Table 3.1.

**Table 3.1** Comparison of crystallinity structure parameters of PPTA and TR-PPTA.

| **(hkl)** | **2θ (°)** | **FWHM (°)** | | **D (nm)** | | **$X_c$ (%)** | |
|---|---|---|---|---|---|---|---|
| | | Kevlar™ | TR-Kevlar™ | Kevlar™ | TR-Kevlar™ | Kevlar™ | TR-Kevlar™ |
| (110) | 20.5 | 1.69 | 1.72 | 5.0 | 4.9 | 76.8 | 78.4 |
| (200) | 22.9 | 1.59 | 1.61 | 5.3 | 5.3 | | |
| (004) | 29.1 | 2.93 | 2.75 | 2.9 | 3.1 | | |
| (121) | 38.0 | 3.14 | 3.38 | 2.8 | 2.6 | | |
| (213) | 31.5 | | 0.16 | | 53.9 | | |
| (116) | 45.3 | | 0.24 | | 37.5 | | |

After treatment, the value of FWHM of (110), (200) and (121) peaks slightly increases, therefore crystalline size decreases. In the TR-Kevlar™ sample, the new peaks appeared at 31.5 and 45.3°, which are related to the (213) and (116) planes, respectively. These peaks were first reported in this study and were indexed according to the comparative study of Rutledge et al. [95]. Zheng et al. have reported an amorphous peak that corresponds to 45°, however this peak is broad and quite weak [100]. The crystalline sizes of these peaks that appear after treatment were calculated as 53.9 and 37.5 nm. The XRD data suggested that the crystallinity of Kevlar™ improved due to the repaired CO bonds in the amide group, which is consistent with the results obtained from the FT-IR spectra. The hypothesis is that, when crystalline sizes are taken into account, the newly created crystals in the skin region become more dominant. The general crystallinity indices of Kevlar™ and TR- Kevlar™ are 76.8 and 78.4%, respectively.

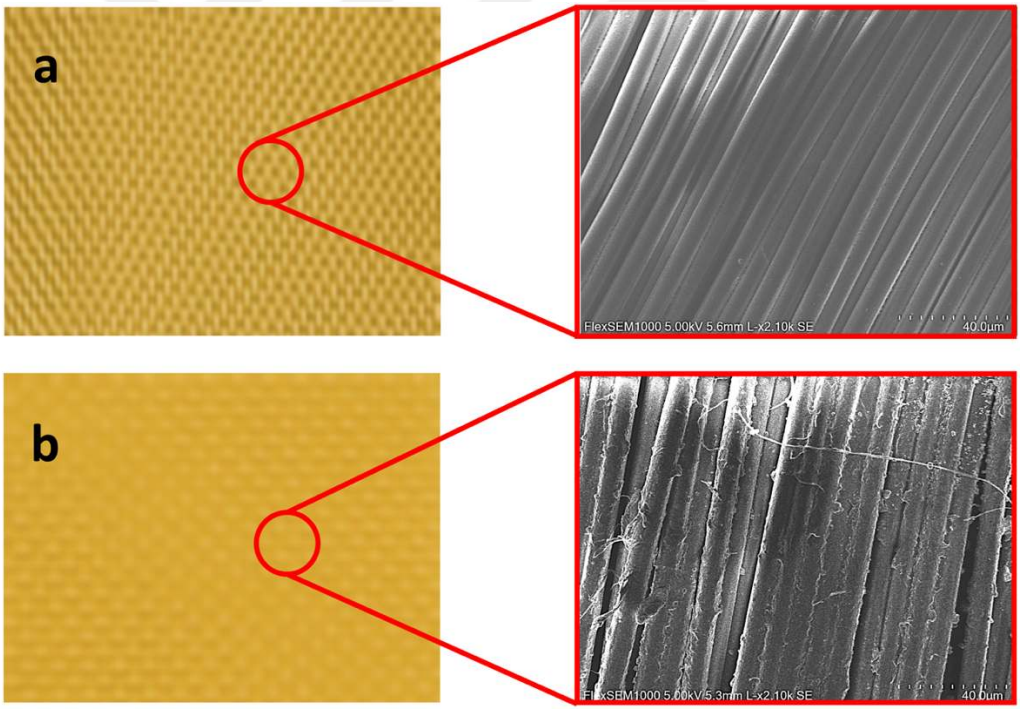


**Figure 3.4** FE-SEM images of the a) treated and b) untreated PPTA surface with solvents.

Surface morphology of the samples was examined by field emission scanning electron microscopy. The untreated fibers have a smooth surface, and the treated fibers were

scraped with a rough surface in Fig. 3.4. The treatment caused the re-crystallization on the surface and the establishment of interchangeable bonds and led to a relatively rough surface in the photographs. Alcohol, aldehyde, amine, AE and some aprotic solvents can break hydrogen bonds in the amorphous regions of polymers [101]. Amorphous and crystalline regions exist together in the structure of Kevlar™. The outer surface and core parts of the material differ in terms of crystallinity, orientation level and number of voids. The reason for this is that the core region has sufficient time for crystallization due to the slow cooling rate, and the chain ends do not have sufficient time for crystallization due to rapid cooling. For this reason, the outer surface is generally the region where crystallization is low and amorphous structures are abundant [102]. Solvents such as AE and EtOH can break the weak bonds in this amorphous structure and cause rearrangement by increasing the mobility of the polymer chains in the amorphous region on the surface.

## 3.2 ZnO Coating and Gas Sensor Performance

### 3.2.1 Crystallinity of ZnO seed layers and ZnO Nanostructures

Fig. 3.5a displays the XRD patterns of the ZnO seed layer applied onto Kevlar™ fabric using the ultrasonic bath method for varying durations. The peaks observed in the coated Kevlar™ fabric substrate align with existing literature, with diffraction peaks at (100), (002), (101), (102), and (110) corresponding to the hexagonal wurtzite structure of ZnO (JCPDS, No.36-1451) [93] [103]. As the ultrasonic bath time increased, the ZnO seed layer on the fabric and the peak intensity increased in direct proportion. The most prominent XRD peaks were seen in the 10 and 20 min ultrasonic bath processes.

Fig. 3.5b shows the XRD peaks of ZnO nanostructures coated with the hydrothermal method on the Kevlar™ fabric surface after the seeding process. As in the seed layer, a hexagonal wurtzite ZnO structure is observed, which is compatible with the literature (JCPDS, No.36-1451). The density and morphology of the ZnO rods formed on the fabric surface varied per unit area depending on the duration of the seeding process. This variability is reflected in different intensities of the ZnO peaks, as shown in Fig. 3.5b. Detailed XRD analysis data is provided in Table 3.2.

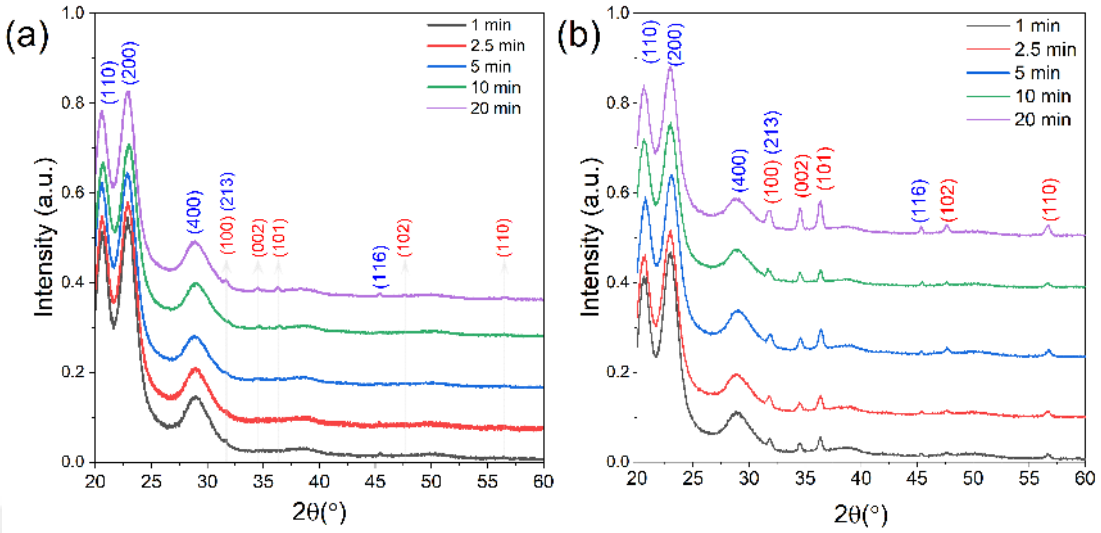


**Figure 3.5** XRD analysis of a) ZnO seed layers and b) ZnO rods.

**Table 3.2** XRD data of ZnO structures.

| Seeding Time (min) | 2θ (°) | FWHM (°) | Height (a.u.) | Area (a.u.) | $D_{002}$ (nm) | Integral breath (a.u.) |
|---|---|---|---|---|---|---|
| 1 min | 34.53 | 0.36 | 567 | 216 | 24.1 | 2.63 |
| 2.5 min | 34.52 | 0.42 | 519 | 229 | 20.7 | 2.26 |
| 5 min | 34.58 | 0.42 | 776 | 344 | 20.7 | 2.26 |
| 10 min | 34.55 | 0.33 | 635 | 222 | 26.3 | 2.86 |
| 20 min | 34.54 | 0.38 | 1457 | 596 | 22.9 | 2.44 |

### 3.2.2 Morphology of ZnO Coatings

To examine the effects of the seed layer, initial ZnO nanostructure growth was performed on the fabric using the hydrothermal method without the seed layer coating. Fig. 3.6 shows the images of ZnO nanostructures grown on fabric at different temperatures and times without the seed layer. Sparse, non-homogeneous, and disorganized rod orientation clearly shows that an inefficient coating was achieved.

The absence of a seed layer on the surface before the ZnO nanostructure growth posed a disadvantage for the nucleation step. Since the nucleation step could not start homogeneously on the surface, the ZnO nanostructure growth process took place in a sparse and inhomogeneous form. Nucleation and nanostructure growth are closely tied to the presence of a seed layer on the surface [104] [105]. The purpose of creating a ZnO seed layer is to facilitate the growth of ZnO structures via the hydrothermal method by creating nucleation centers on the substrates. In addition, the seed layer enables epitaxial growth by eliminating the lattice mismatch effect between ZnO structures and substrates [106]. The seed layer formed on Kevlar™ fabric offers numerous nucleation areas during the ZnO nanostructure growth process with the hydrothermal method.

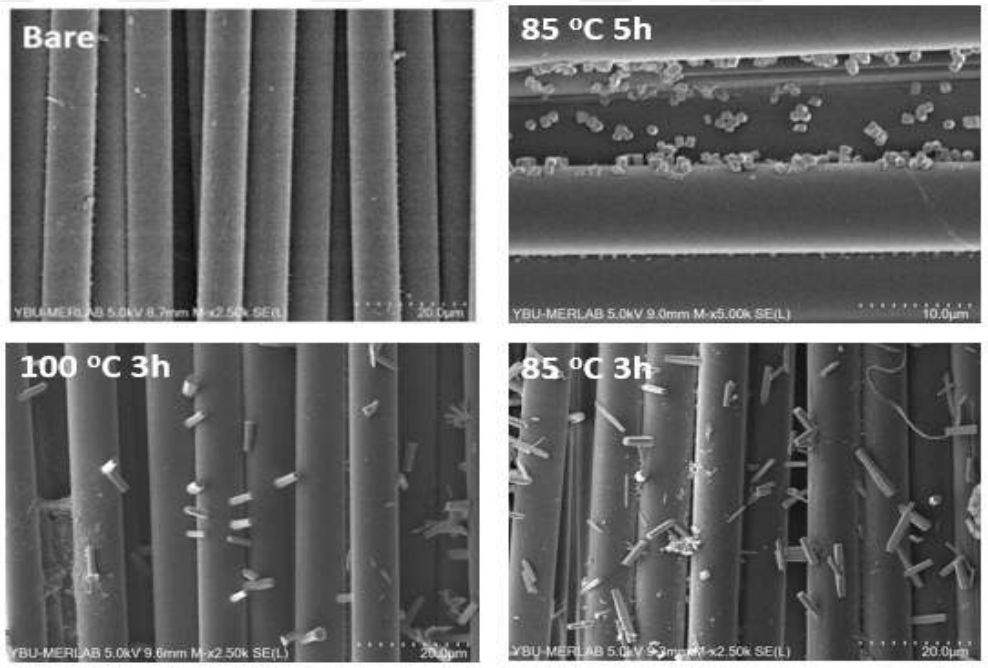


**Figure 3.6** SEM images of the ZnO-coated Kevlar™ fabrics without seed layer.

ZnO nanostructures were grown by the hydrothermal method at 85°C for 5 h on the seed layer produced by the ultrasonic bath method at different periods of time. The morphology and distribution of the ZnO on the Kevlar™ fabric were examined by SEM. It is clearly seen in Fig. 3.7 that the rod distribution on the surface is highly affected by the ZnO seed layer properties. Additionally, the length and width distributions of the nanostructures are shown in Fig. 3.8. Increasing the seeding time

resulted in a more homogeneous and denser distribution of rods. This is because longer seeding times lead to the formation of more extensive ZnO seed layers on the fabric surface, providing a larger surface area for ZnO structures to grow. Fig. 3.9 shows the ZnO seed layer EDS results indicating the ZnO wt% on the surface depending on time. For the seeding process, as the ultrasonic bath treatment time increases, the amount of ZnO on the fabric surface increases. For this reason, although the parameters such as temperature, time and solution were kept same in each sample during the hydrothermal method growth process, the rod distribution and morphology on the surface varied depending on the seeding time. As the seeding time increased, the nanorods formed on the surface turned into flake-like structures.

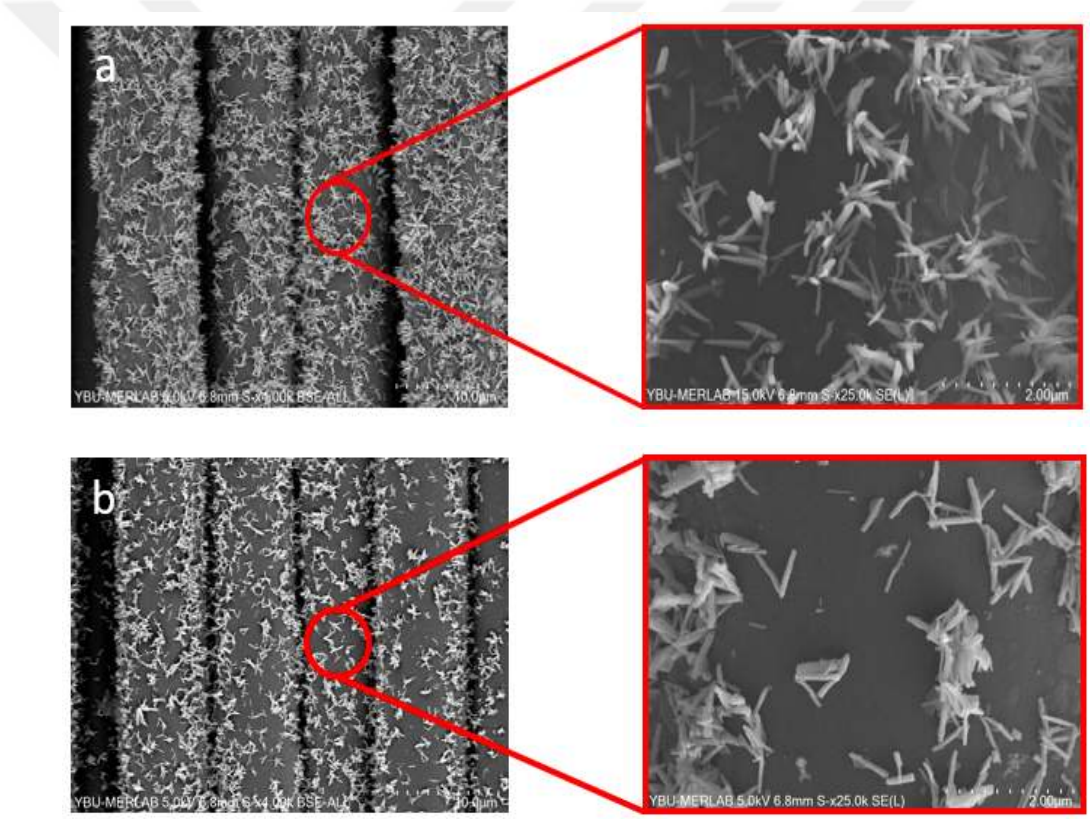


**Figure 3.7** SEM images of hydrothermally synthesized ZnO coatings on a) 1-min seeded, b) 2.5-min seeded, c) 5-min seeded, d) 10-min seeded, and e) 20-min seeded Kevlar™ fabrics.

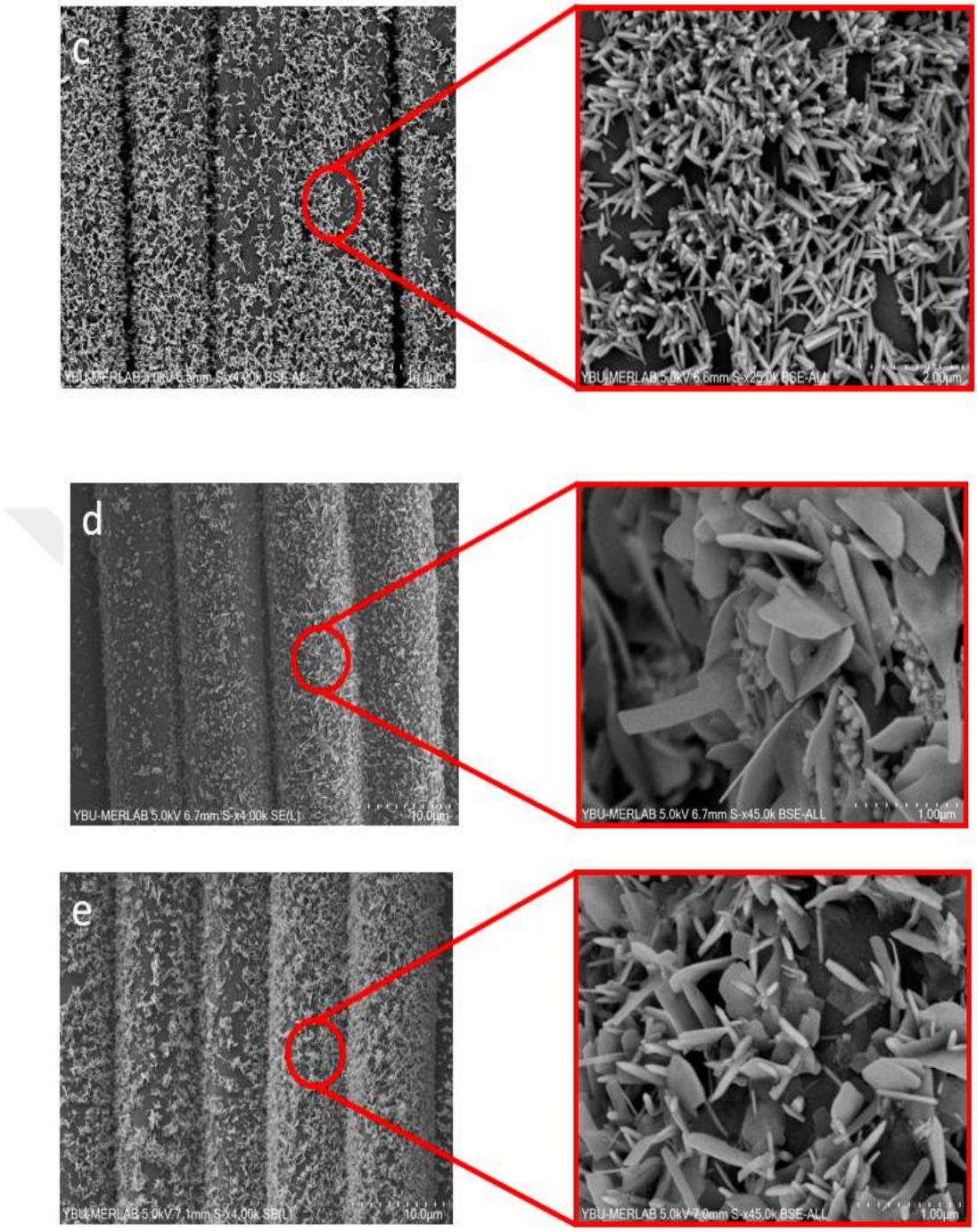


**Figure 3.7** (continued): SEM images of hydrothermally synthesized ZnO coatings on a) 1-min seeded, b) 2.5-min seeded, c) 5-min seeded, d) 10-min seeded, and e) 20-min seeded Kevlar™ fabrics.

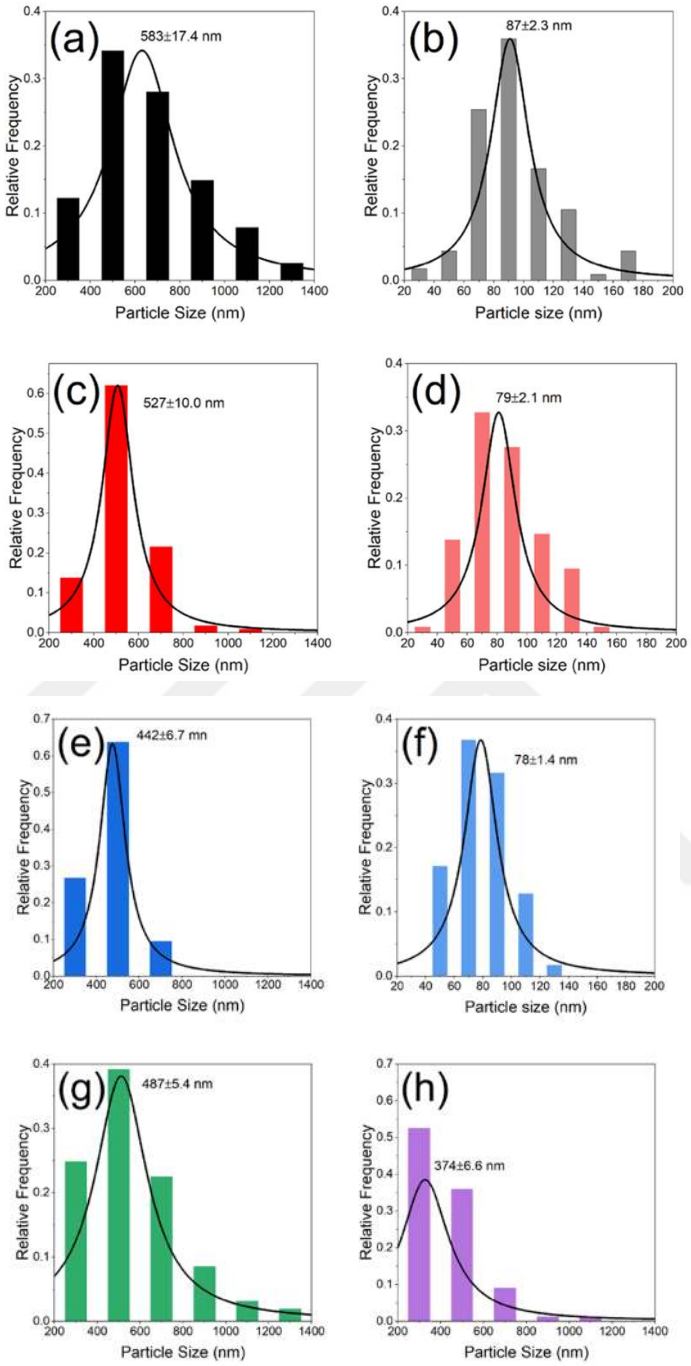


**Figure 3.8** The length and width distributions of 1D zinc oxide nanorods for ultrasonication seeding times of a, b) 1 min, c, d) 2.5 min, and e, f) 5 min. Additionally, width distributions of 2D nanosheets for ultrasonication seeding times of g) 10 min and h) 20 min.

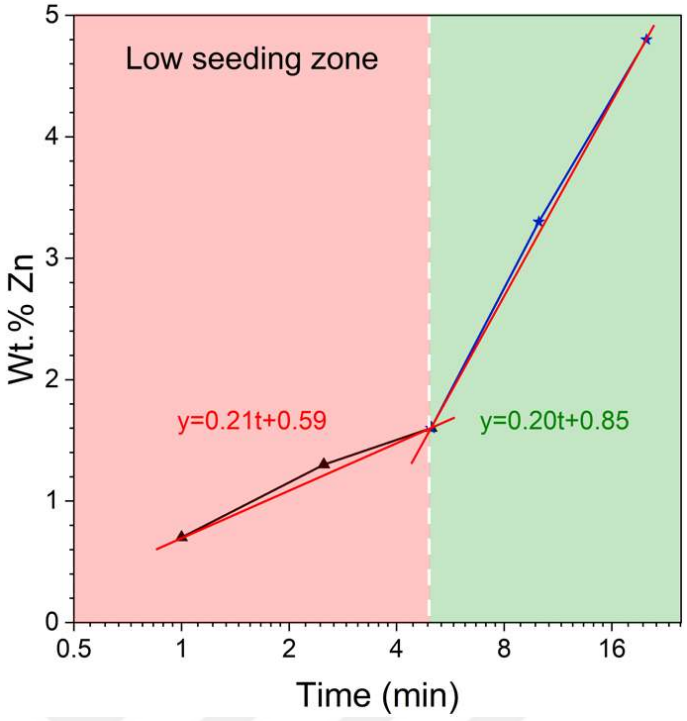


**Figure 3.9** Kevlar™ fabric ZnO seed layer wt %-time EDS results graph.

**Table 3.3** Data regarding the dimensions of ZnO rods vs. seeding time.

| Seeding Time | Length (nm) | Width (nm) | Aspect ratio |
|---|---|---|---|
| 1 min | 625 | 90 | 6.70 |
| 2.5 min | 505 | 80 | 6.67 |
| 5 min | 475 | 78 | 5.67 |

The average ZnO nanorod length on the fabric surface decreases as the seeding time increases. As a result of 1 min of seeding, ZnO nanorods with an average length of approximately 625 nm were produced, while this length was 505 nm for 2.5 min, and 475 nm for 5 min. Depending on the duration of the seeding, the width, length and aspect ratio values of the ZnO rods on the Kevlar™ fabric surface are given in Table 3.3 and distributions are given in Fig 3.8. The sample with a larger aspect ratio possesses a greater surface area for rod formation. This can be advantageous for gas

sensors as it increases the contact surface, potentially enhancing sensitivity. However, it is important to note that a continuous and homogeneous seed layer plays a crucial role in the electrical conductivity of the substrate where the rods are grown. This conductivity contributes significantly to the overall performance and functionality of the sensor. Another important parameter affecting the gas sensor properties is the ability of the surface on which the rods are grown to provide holistic conductivity. In the samples seeded for 10 min and 20 min, as the seeding time increases, it was observed that the nanorods formed on the surface turned into flake-like and were coated very homogeneously all over the surface. The SEM image of the distribution of nanostructures on the Kevlar™ fabric surface at the same magnifications is shown in Fig. 3.10. Nucleation and rod formation areas varied depending on the seeding time. The surface area required for nucleation increased with seeding time. Guillemin et al. produced ZnO nanowire by chemical bath deposition after coating a seed layer on a Si substrate. They noted that the thickness of the seed layer increased and the density of ZnO nanowires per unit area increased while their lengths decreased [104]. Boercker et al. argued in their studies that, when ZnO nanowire is grown by chemical bath deposition method, the chemical components in the solution should be limited by mass transport. This leads to an inverse relationship between the average length of ZnO nanowires and their density per unit area [107]. Therefore, in parallel with these explanations, the rod density on the fabric surface increased, and since the solution amount and concentration were constant, the average length of the ZnO rods formed in the 5 h production period was shortened.

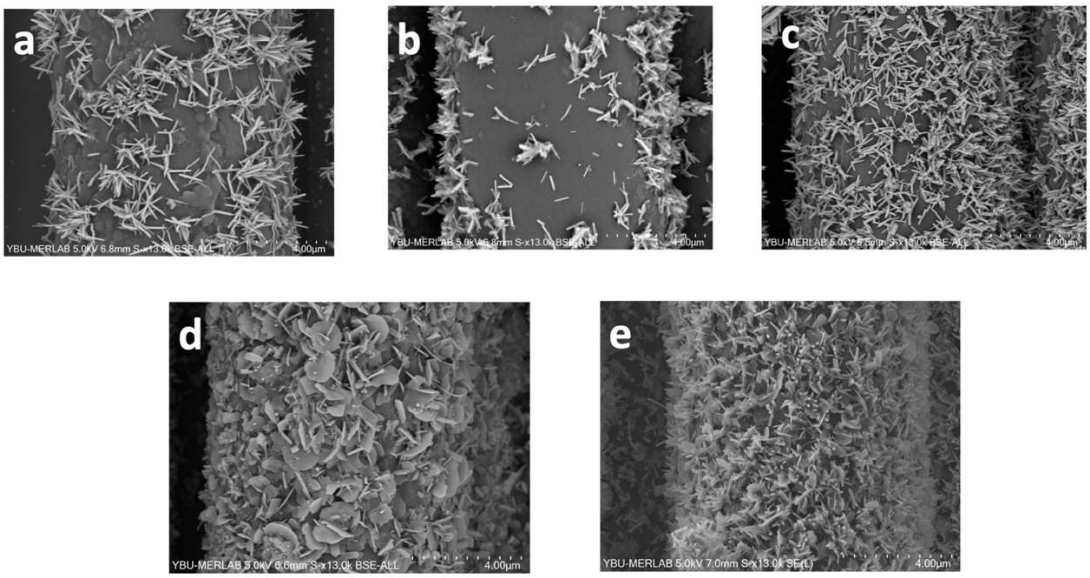


**Figure 3.10** SEM image of the distribution of nanostructures on the Kevlar™ fabric surface at the same magnifications a)1 min, b) 2.5 min, c) 5 min, d) 10 min, e) 20 min.

The primary factors affecting rod length are typically the amount of ZnO source in the solution and the duration time of the growth process [108]. However, in this study, despite maintaining consistent solution content and amount across all samples, the average rod length changed due to changes in nucleation area resulting from differences in seeding time. As the seeding time and consequently the surface area increased, the likelihood of more nucleation and rod formation also increased. This led to the production of denser, more homogeneous, and shorter rods.

As seen in Fig. 3.7d and 3.7e, flake-like ZnO as well as ZnO nanorods are seen in the samples where 10 and 20 min seeding processes were employed. This situation is directly related to the amount of seed layer on the Kevlar™ fabric surface. Hexamethylenetetramine plays an important role as an $OH^-$ source in the hydrothermal process. As a result of the reaction of $Zn^{2+}$ and $OH^-$ with aqueous solution, growth units of ZnO are formed. It is known that supersaturation, which is necessary for crystal growth, is also effective in morphology formation. During the hydrothermal process, $OH^-$ ions play a major role in the morphological formation of ZnO [109]. Zhang et al. observed that when the main component ratios in the hydrothermal

solution changed, the ZnO morphology changed from nanorod to nanoplate with the increase of $OH^-$ concentration in the environment. The main reason here is the anisotropy of ZnO crystals and the growth of the crystal towards the non-polar surface. In this study, the presence of different amounts of ZnO seed layer on the Kevlar™ fabric affects the nucleation and crystallization stages [103]. On fabric surfaces with sparse seed layer coating, nucleation and nanostructure growth step occurs locally. The nucleation and subsequent nanostructure growth process exhibited a linear pattern on the surface with a denser seed layer, while appearing scattered and sporadic on the surface with a sparser seed layer. In addition, since the nucleation and crystal growth process is faster on surfaces with a denser seed layer, it is being thought that more reactions occur at the same temperature, time and concentrations. According to this hypothesis, it is assumed that the repeated chemical reactions occurring in the hydrothermal process lead to the generation of more $OH^-$ ions. These ions play a crucial role in the simultaneous formation of both rod-like and flake-like structures.

### 3.2.3 Gas-sensing analysis

The gas detection mechanism in the ZnO gas sensor is a two-stage process as shown in Fig. 3.11. In the first stage, the oxygen in the air is adsorbed by the sensing surface. Adsorbed oxygen molecules become ionized by capturing electrons in the conduction band of ZnO. Electron depletion layer (EDL) expands and electrical resistance increases on the ZnO surface, whose electrons in the conduction band are held by oxygen ions. In the second stage, $NH_3$ gas molecules adsorbed by the surface react with oxygen ions, causing the electrons to be released back into the conduction band of ZnO and the electrical resistance on the surface to decrease [110] [111] Detection reactions of $NH_3$ gas by the ZnO gas sensor:

$$O_2 + e^- \rightarrow O_2^- \tag{3.3}$$

$$4NH_3 + 3O_2^- \rightarrow 4N_2 + 6H_2O + 3e^- \tag{3.4}$$

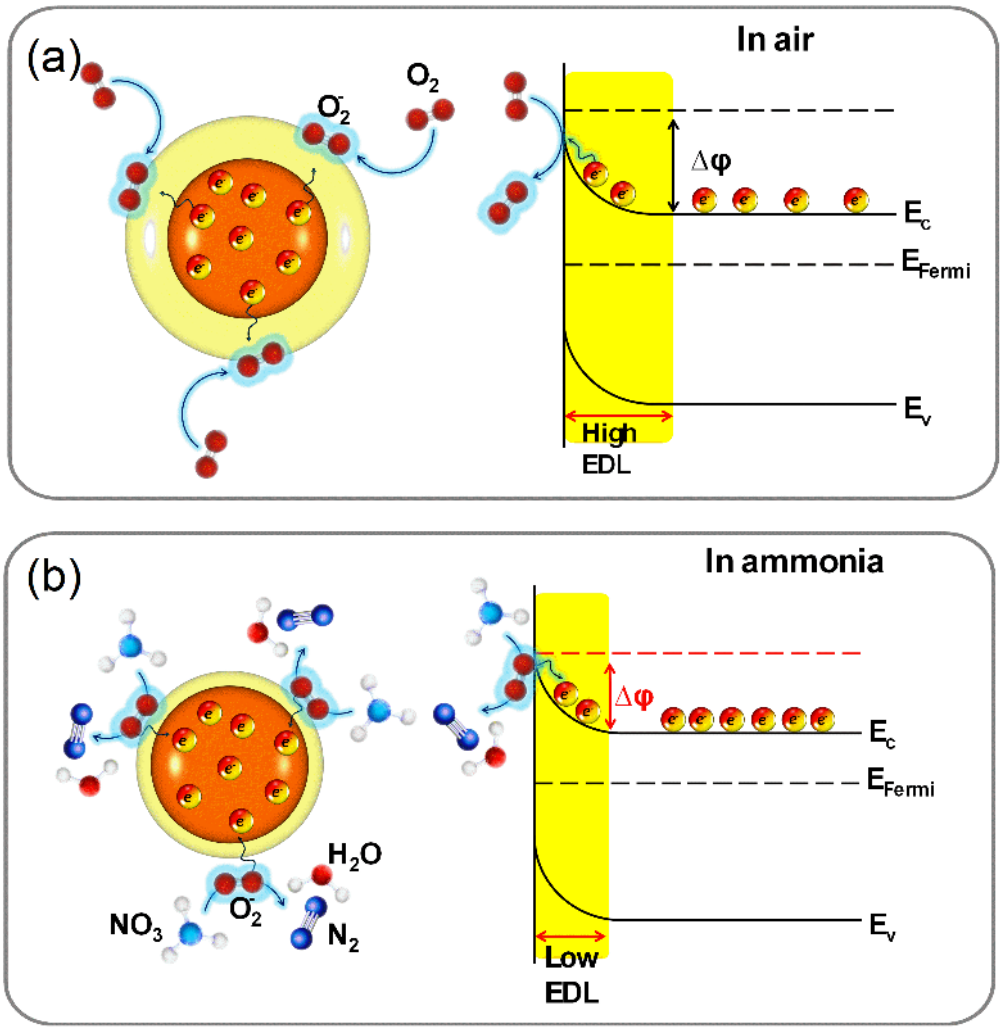


**Figure 3.11** Schematic representation of the sensing mechanism in ZnO nanoparticles toward air ammonia.

The fabricated sensors were operated at different temperatures in an atmosphere containing 50 ppm of $NH_3$ gas with repeated exposure and recovery cycles. In this context, during the measurements, the sensors were put under exposure to the gas for 5 min and then allowed to recover in dry air for 5 min starting from RT and extending in steps of 15 °C up to a specific temperature at which a clear drop down in response was noted. The sensor produced on Kevlar™ fabric substrate is shown in Fig. 3.12. The sensing response (S) of the fabricated sensors was subsequently evaluated at each temperature using the relation [112];

$$S = \frac{|\Delta R|}{R_g} \times 100 \quad (3.5)$$

where ΔR is the difference between the initial resistance of the sensor in air ($R_a$) and its extreme resistance in exposure to the target gas ($R_g$). Fig. 3.13 presents the obtained transient resistance signals and the corresponding estimated responses of the sensors at each operating temperature. Functioning as chemiresistive sensors, the fabricated sensors responded to the presence of the gas by a change in their resistance. More precisely, when subjected to $NH_3$ at a suitable temperature, the sensors displayed a reduction in resistance. This decrease in resistance is in line with the established literature [113] [114] [115] and is anticipatable due to the inherent n-type conductivity of the sensing material and the strong reducing properties of the target gas. At RT, the fabricated sensors struggled to effectively detect the existence of 50 ppm of $NH_3$ gas, with the exception of the N20 sensor. Impressively, at RT, the N20 sensor showcased an acceptable response limit of about 20% with a satisfactory recovery level upon gas termination. However, it can be said that the sensors recorded their first reliable response above 100 ℃.

**Figure 3.12** The sensor produced on Kevlar™ fabric substrate.

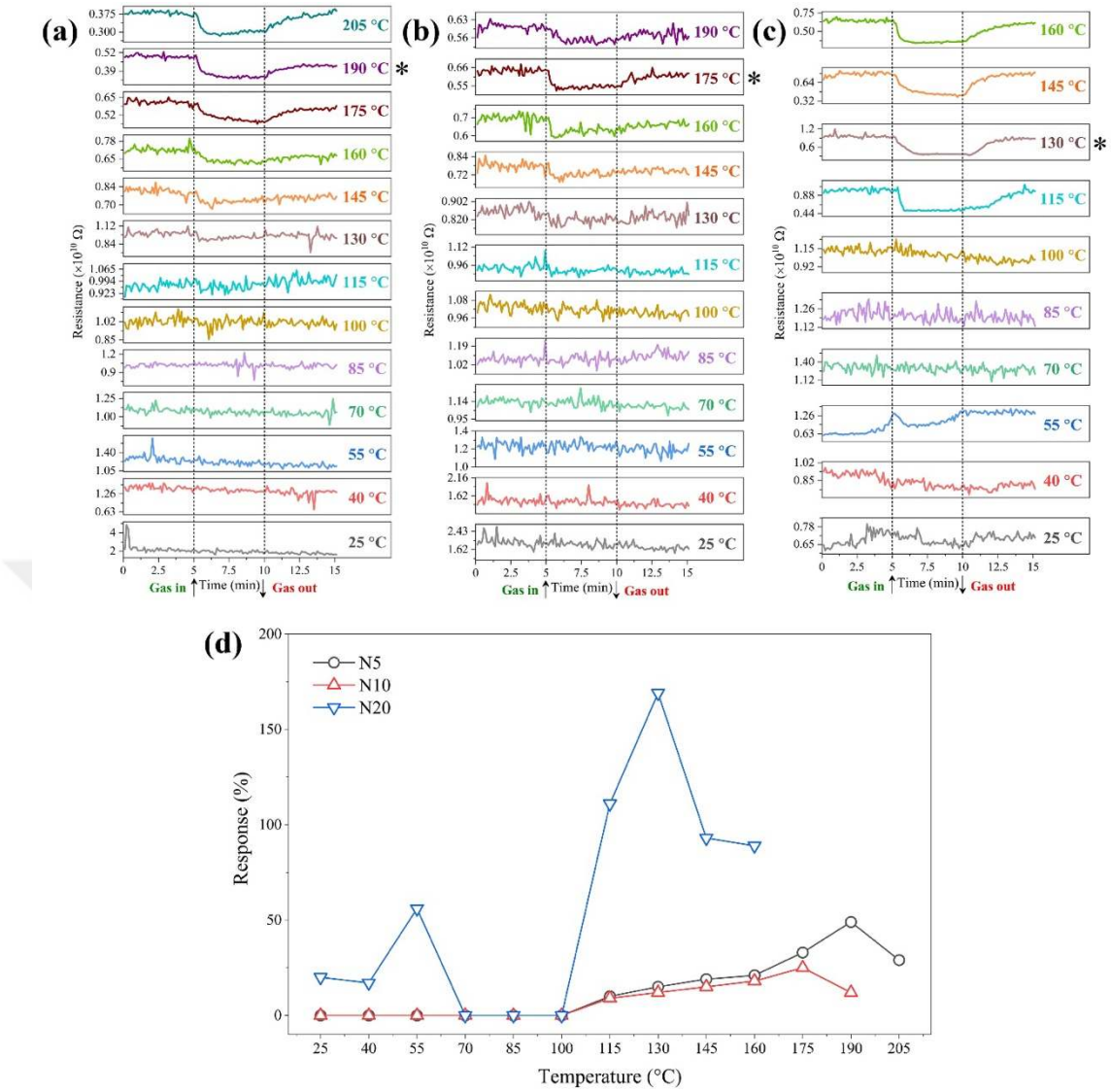


**Figure 3.13** Transient resistance plots of the (a) N5, (b) N10 and (c) N20 sensors versus temperature with exposure to 50 ppm of $NH_3$ gas (the optimal operating temperature of each sensor is marked by an asterisk *). (d) Temperature-dependent response of the sensors estimated using the corresponding transient plots.

The alterations in the electron depletion layer and conduction channel caused by changes in morphology are illustrated in Fig. 3.14. Li et al. observed that the selected volume of 2D nanostructures (nanoflakes) and 1D nanostructures (nanorods) had respective values of 2.8a/V and 1.3a/V $nm^{-1}$ [116].The ratio of surface area to volume of the 2D nanostructures is approximately 2.2 times than that of the 1D nanostructures, this may make 2D structures superior in terms of sensitivity. The higher surface area

to volume ratio provides more space for adsorption of target gas molecules and improving the sensitivity and response velocity by accelerating charge accumulation [117]. The conduction channel becomes narrower due to the increase in the high surface-area-to-volume ratio. This enhances the rate at which the resistance changes on the surface of the sensor. Efficient gas-surface contact facilitates the detection of gas molecules, especially at lower temperatures. Therefore, the surface area/volume ratio interacting with the target gas is very important in defining the optimum operating temperature of gas sensors [118] [119].

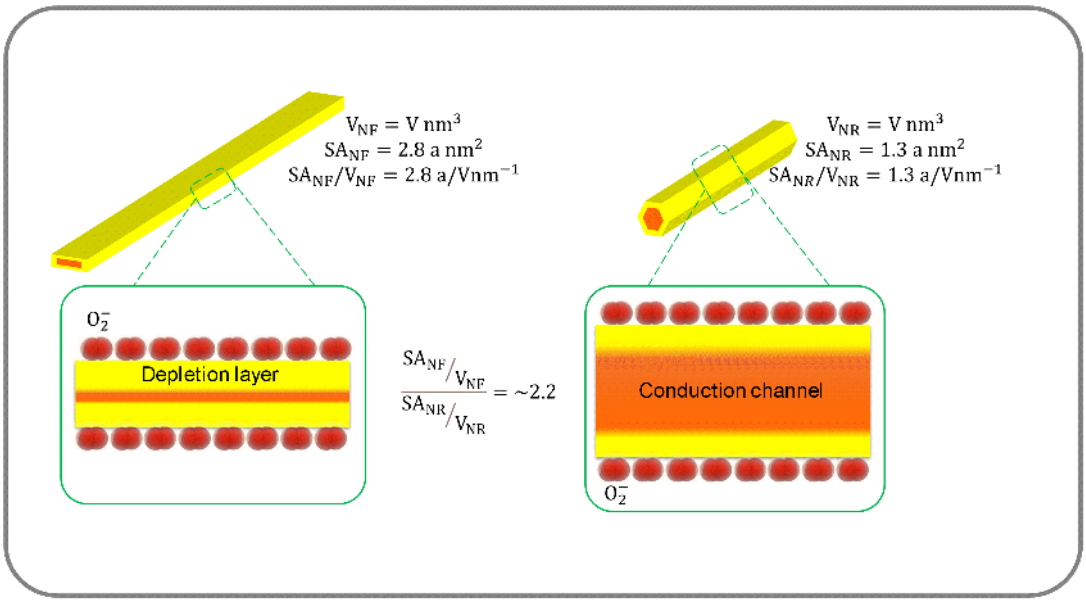


**Figure 3.14** The alterations in the electron depletion layer and conduction channel caused by changes in morphology.

With the increase in temperature, the response of the sensors increased gradually and peaked at a temperature famously known as the optimal operating temperature beyond which the response declined again. Specifically, the N5 sensor reached this maximum of sensing response at 190 ℃, the N10 sensor at 175 ℃, and the N20 sensor at 130 ℃. These temperatures can be deemed moderate given that the majority of MOS-based chemiresistive gas sensors typically perform within the range of 200 to 400 ℃ [120] [121] [122]. The sensors registered the following responses at their respective optimal operating temperatures: 49% for the N5 sensor, 25% for the N10 sensor and 169% for the N20 sensor. Certainly, judging by the optimal temperature and corresponding

response, it is evident that the N20 sensor demonstrates the most exceptional performance among other sensors. The gas sensing process involves gas adsorption, charge change, and gas desorption steps. However, $O_2$ adsorption on the surface is also crucial for sensor performance, particularly in ZnO gas sensors. The morphology of ZnO directly influences $O_2$ adsorption and sensor performance. Nanoflake structures on the sensing surface offer larger specific surface area than nanorod structures. Li et al. reported that the specific surface areas of zero, one and two-dimensional nanostructures with similar volume are reported as 1x, 1.3x and 2.8x, respectively. In simpler terms, the 2D nanostructures have a greater surface area compared to the 1D nanostructures when they have identical volumes [116]. In this way, nanoflake structures contribute to sensor performance by adsorbing more oxygen than nanorod structures in the gas sensing process. This is because each crystal surface has a (unique) different number of dangling bonds. As the number of dangling bonds on the sensing surface increases, oxygen ionization increases, and sensor performance improves [123]. Qin et al. studied morphology-dependent gas sensor performance by producing ZnO gas sensors in various shapes like disc, prismoid, prism, and pyramid morphologies. They found that the gas sensor with a disc morphology exhibited remarkably high performance. This is attributed to the (0001) polar ZnO crystal surfaces present in the disc morphology, which provide more active sites for $O_2$ adsorption [124]. In a study made by Li et al., they synthesized high surface area sensors and discovered that the sensor sensitivity to $H_2$ gas increased linearly with increasing surface area of the sensor [125]. Similarly, $NH_3$ sensors containing more ZnO nanoflakes demonstrated superior performance, likely due to increased surface area and active sites for gas adsorption [124].

Additionally, at their optimal operating temperatures, the response time (the duration it takes for the sensor to reach 90% of its maximum reading) and the recovery time (the duration it takes for the sensor to revert to 90% of its initial reading) are as follows: 46/– s for the N5 sensor, 15/50 s for the N10 sensor and 91/176 s for the N20 sensor. It is notable that the N10 sensor was the quickest in responding to the presence of the gas and in recovering in the absence of the gas compared to the others.

Besides that, the rise in temperature led to a reduction in the resistance of the sensing films, in line with the anticipated semiconductor behavior induced by temperature. Nevertheless, possibly due to substrate effects, the decrease in resistance was not substantial with a maximum change of approximately $10^2$ Ω with the temperature increasing from 25 to 160℃. The authors attribute this behavior to the specific characteristics and thermal properties of the substrate material. For example, in the case of a glass substrate, the resistance of the ZnO sensing element usually shows heightened sensitivity to temperature, resulting in significant changes even with slight temperature increases [126]. Alternatively, when the substrate is a fabric, as is the case here, the resistance of the sensing film experiences a subtle decrease with rising temperature.

To check the responsiveness of the sensors towards various gas concentrations, they were exposed to 1, 5, 10, 20, 50 and 100 ppm of $NH_3$ gas in a series of exposure-recovery cycles at their optimal operating temperature. The obtained results are given in terms of resistance change in Fig. 3.15a-c. Evidently, the escalation in gas concentration corresponded to a heightened alteration in the resistance of the sensors. The degree of linearity in the relationship between gas concentration and response holds significant importance for commercial applications. Notably, the N20 sensor demonstrated the most favorable linearity, with a coefficient of determination (COD) or $R^2$ of 0.863, surpassing the performance of other sensors in this aspect. For a better comparison, the dynamic plots of all the fabricated sensors are also superimposed in terms of their sensing response (Fig. 3.15d). It can be seen that the response displayed by the sensors under dynamic measurements at a 50 ppm concentration of $NH_3$ gas is akin to the response observed in earlier temperature-dependent measurements (Fig. 3.13d). This suggests a certain level of stability in the fabricated sensors, indicating their capacity to consistently produce reliable measurements. Additionally, it is noteworthy that the baseline levels of the sensors remained consistent at identical temperatures (Fig. 3.13a-c and Fig. 3.15a-c). This uniformity in baseline levels further emphasizes the stability of the fabricated sensors across varying conditions, contributing to their reliability and consistency in measurement outcomes.

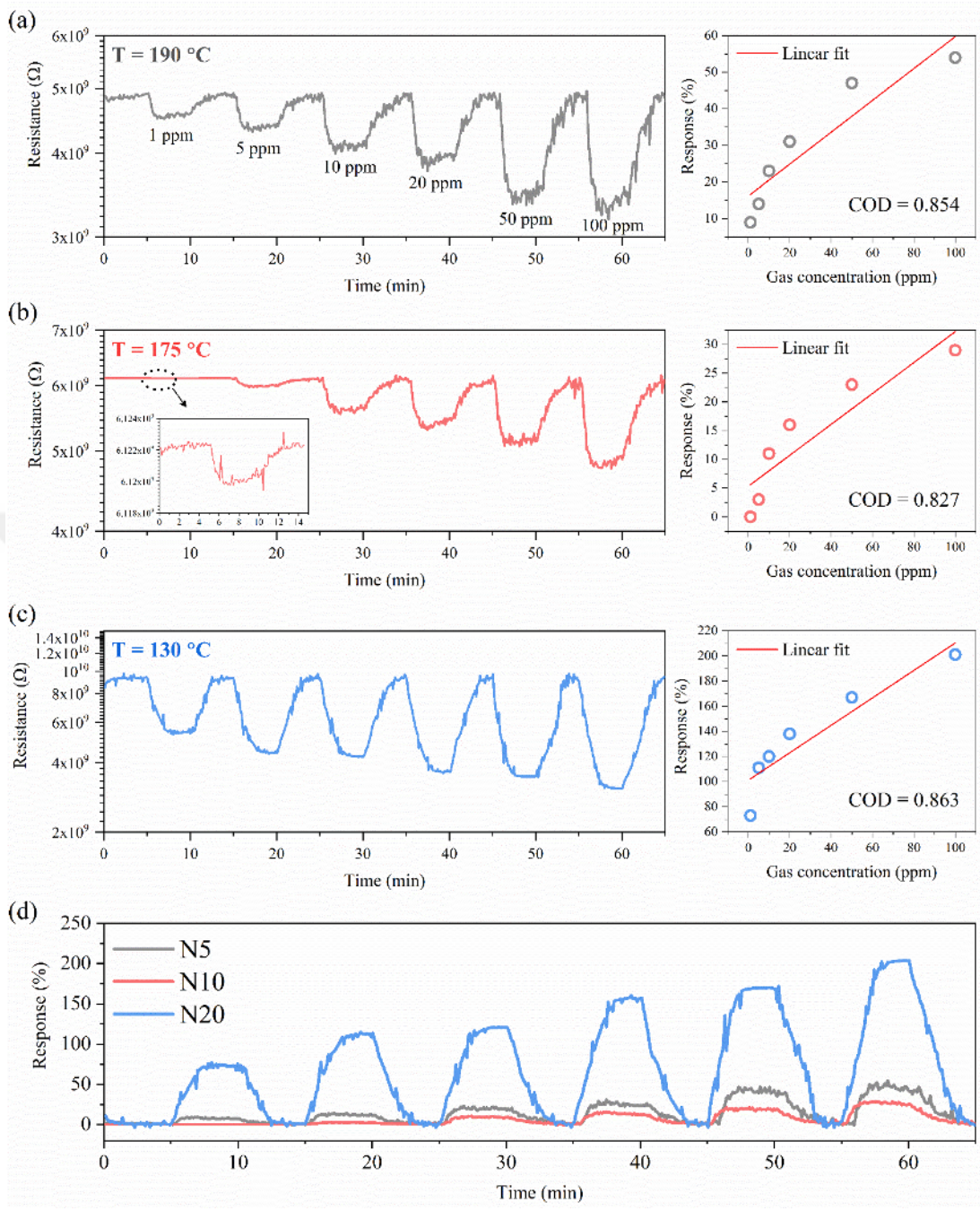


**Figure 3.15** Dynamic and calibration plots of the (a) N5, (b) N10 and (c) N20 sensors in terms of resistance at the optimal operating temperature for each sensor. (d) Superimposed dynamic plots of the sensors in terms of their sensing response.

Other properties like repeatability, endurance under prolonged exposures and selectivity are also critical in the evaluation of sensors for commercial applications. These aspects contribute significantly to the overall performance and reliability of the

sensors in real-world scenarios, ensuring their suitability for diverse and demanding applications. To assess repeatability, the sensors were put in four repetitive exposure-recovery cycles by exposing them to a fixed gas concentration (50 ppm) at their optimal operating temperature (Fig. 3.16). Following a marginal decrease in response during the initial exposure-recovery cycle, the signals of the sensors nearly stabilized during later cycles. The observed stabilization in the sensors' signals, even after the initial response drop, suggests a degree of short-term stability. This indicates that, within the defined conditions of repetitive exposure-recovery cycles at a fixed gas concentration and optimal operating temperature, the sensors exhibit stability to a certain extent over the short term. To evaluate the capacity of the sensors to withstand exposures to the gas for an extended period, they were operated in an atmosphere with 50 ppm $NH_3$ for a 15-min period before terminating the gas and allowing them to undergo the recovery phase (Fig. 3.16). Except for the N5 sensor which showed a slight poisoning phenomenon before stabilizing, all other sensors showed promising endurance to prolonged exposures to $NH_3$ gas. This observation underscores the robustness and resilience of the majority of the sensors in maintaining stable performance under prolonged exposure conditions over time, especially the N20 sensor. Once again, the baseline levels of the sensors are observed to be similar compared with the results obtained from separate experiments conducted at similar temperatures, as illustrated in both Figs. 3.13 and 3.15. This consistency in baseline levels across different experiments reinforces the reliability and reproducibility of the sensors' performance under similar operating temperature conditions. To check the selective ability of the sensors towards different gases, individual exposures were conducted for 50 ppm of $H_2$, $CO_2$ and $NO_2$ gases at the respective optimal operating temperatures. From the obtained transient plots, the response of the sensors to each gas was estimated using the same formulation (Eq. 3.3) that was used to estimate the response to $NH_3$ gas. The outcomes are visually presented in radar plots in Fig. 3.16. The comparative analysis depicted in the radar plots reveals that the sensors exhibited minimal responses to other gases in contrast to their notable response to $NH_3$ gas. These results underscore the high selectivity of the fabricated sensors for $NH_3$ gas, further emphasizing their suitability for targeted applications in $NH_3$ detection. Also, the sensors' selective responses to $NH_3$ gas, as demonstrated through controlled

exposures and stability assessments, highlight their potential effectiveness and reliability in scenarios where accurate detection and monitoring of ammonia gas are essential.

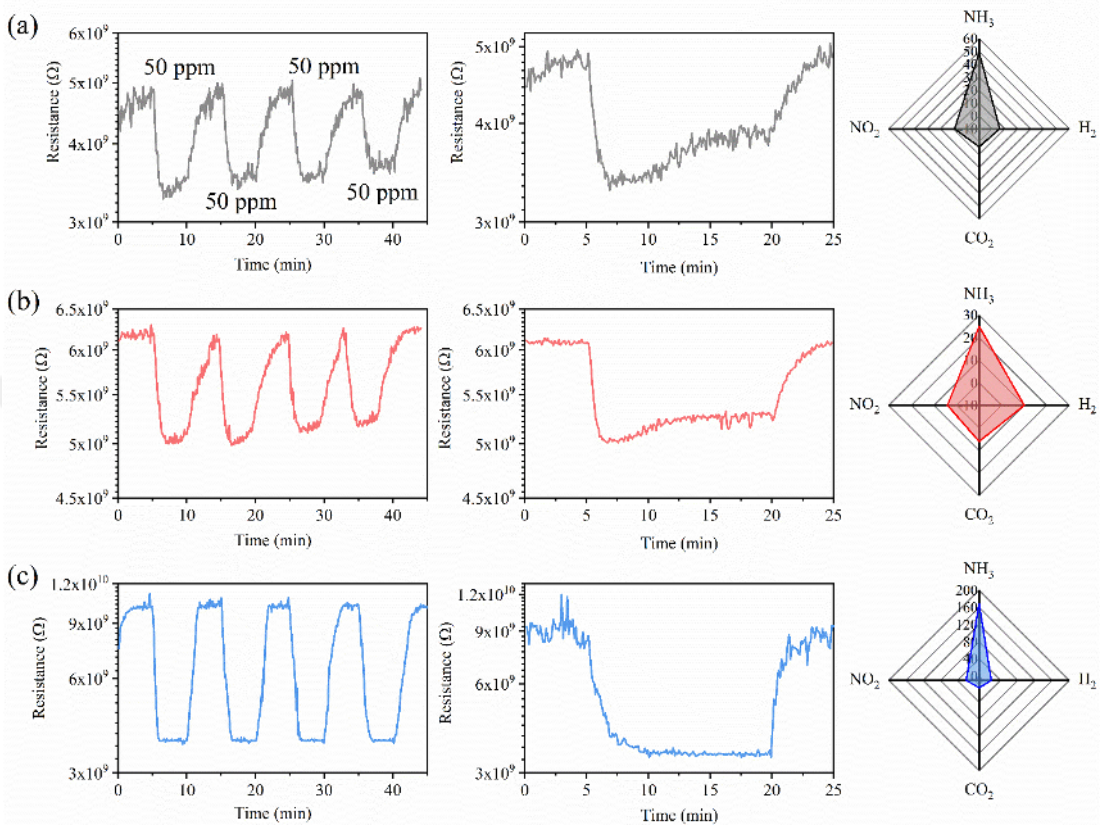


**Figure 3.16** Repeatability (left), long-exposure endurance (middle) and selectivity properties (right) of the (a) N5, (b) N10 and (c) N20 sensors at the optimal operating temperatures.

**Table 3.4** Review of the most recent ZnO-nanostructure based gas sensors reported in the literature.

| Materials | Fabrication | | | Sensing performance | | | | |
|---|---|---|---|---|---|---|---|---|
| | Type | Substrates | Production Method | Working Temperature (°C) | Detection Range (ppm) | $t_{res}/t_{rec}$ | Response (Ra/Rg) or sensivity* | Refs. |
| ZnO nanoparticles | Thin film | Si wafer | Spin coating | 150 | 50–600 | 160s/660s | 57.5% | [127] |
| ZnO nanoparticles | - | Glass | Drop casting | 100<br>25 | 1260 | 25s/~33s<br>~32s/22s | 1.9%<br>12% | [128] |
| ZnO Nanowire | Thin film | Glass | SILAR | 32 | 50 | -/- | 80.2% | [129] |
| ZnO Nanowire | Thin film | Si wafer | CVD | 300 | 1000 | 100s/100s | 22.50% | [130] |
| ZnO Nanowire | - | ITO<br>µHP chips | Hydrothermal | 350 | 200<br>50<br>10 | 3.8 min/18.4 min<br>6.4 min/19.9 min<br>7.4 min/21.5 min | 4.2*<br>2.3*<br>1.5* | [131] |
| ZnO Nanorod | - | Au/Glass | Hydrothermal | 150<br>RT | 500 | -/- | 8* | [132] |
| ZnO nanorod | Thin film | Sapphire | Hydrothermal | 650 | 100 | -/- | 22.6 | [133] |
| ZnO Grain | Thin film | Glass | Spin coating | RT | 400<br>20 | 37s/90 s | 38.5 ± 0.86<br>6.1 ± 0.8 | [111] |
| ZnO nanofiber | PANI/PEO–ZnO nanofiber | Si wafer | Electrospinning | RT | 250 | 245s/153s | 44* | [134] |
| ZnO nanostructures | N5 (rods) | Kevlar fabric | Hydrothermal | 190 | 1-100 | 46s/– s | 49% (50 ppm) | This study |
| | N10 (flakes) | | | 175 | | 15s/50 s | 25% (50 ppm) | |
| | N20 (hybrid) | | | 130 | | 91s/176 s | 169% (50 ppm) | |

A comparison of ZnO-based gas sensors manufactured on various substrates by different production methods and substrates previously reported is shown in Table 3.4. To the best of our knowledge, this study represents a novel approach by utilizing fabric as a substrate for gas sensors, employing the seeding process with ultrasonication, and demonstrating that the seeding duration with ultrasonication influences the nanostructure morphology. Overall performance of the present device is generally better than that of the reported ones; it particularly outperforms them with a higher response. Basically, a higher responsivity is responsible for an improvement in the detectivity of the sensing devices. Morphology transformation (from 1 D to 2D and hybrid) reduces optimum operating temperature, moreover, the hybrid structure exhibits performance even at room temperature. Recovery and response times of the presented sensor exhibits significant improvement when compared to sensors based on nanorod and nanowire-based sensors, however, these values remain lower than nanoparticle and nanograin-based sensors. Finally, the hybrid gas sensor demonstrated a substantial increase in responsivity, with improvements of 245 and 576% comparing to the nanorod and nanoflake sensors, respectively.

# CHAPTER 4

## CONLUSIONS

### 4.1 Kevlar Substrate

In this study, in addition to the cleaning of contaminants on the Kevlar™ surface by AE and EtOH, the changes in the crystal and molecular structure of the fabric molecules were examined. The fact that there is more amorphous structure on the outer surface compared to the core area creates a disadvantage for the nano-coating process on the surface of Kevlar™ fiber fabrics. The presence of crystalline structures instead of amorphous structures on the coating surface is more advantageous for the coating. The reason for this is that adhesion or nucleation steps tend to occur on the crystalline structure, which has a more ordered structure compared to the amorphous structure.

The findings revealed that treatment process significantly affected the characteristics of Kevlar™ fabrics:

- Amorphous chains can re-organize into regular crystal structures in surface regions.
- Since Kevlar™, a polymer-based material, has partially amorphous regions in its structure, specific solvents such as AE and EtOH increased the proportion of crystallinity by reducing the proportion of amorphous regions with weaker bonds.
- Raman and FTIR show the results that there was no structural deterioration, and even after this process, the defects in the CO groups have been removed.
- The XRD results have shown that new crystal orientations have emerged while crystal dimensions are almost preserved. There was a modest development in crystallinity after treatment.
- SEM images show that the crystals re-formed on the surface occur between fibres and surfaces of fibres.

Future studies can be done to expand this treatment work and to investigate the application of time, temperature, and various solvents effects in closed containers.

After this treatment, coatings can be made, and attachment properties can be investigated.

## 4.2 ZnO Morphology and Gas Sensor

In the presented study; the effect of seeding process on ZnO growth in Kevlar™ fabric by hydrothermal method and the gas sensor performance of these nanostructures were examined. SEM images show that the coatings made without the seed layer are sparse, homogeneous and inefficient. The seeding process directly affected the nucleation, morphology and coating quality on the surface. XRD analysis of the ZnO structures formed on the surface after the hydrothermal method, depending on the seeding time, shows that time and peak intensity are directly proportional. According to EDS analysis, the amount of seed layer on the surface increases as time increases. Therefore, the amount of ZnO nanorods per unit area increases up to a certain point. Although the density per unit area increases under constant hydrothermal method conditions and solution concentration, the nanorod lengths shorten and turn into a rod-flake hybrid morphology after 10 min of seeding.

In this case, the importance of the seed layer in the ZnO coating made by hydrothermal method on Kevlar™ fabric is clearly seen. In addition, the seeding process time directly affects the coating density and morphology. Depending on the morphology and coating quality, Kevlar™ fabric ZnO gas sensor performances varied. While only the N20 sensor showed significant performance at RT, maximum detection response temperatures were measured at 190°C for N5, 175°C for N10, and 130°C for N20. At optimum operating temperatures, the N10 sensor had the fastest response time, while the N20 sensor showed the best response performance with a rate of 169%. Considering these results, the gas sensor with flake and rod-flake hybrid structure coated on Kevlar™ fabric stood out with its performance.

**Acknowledgment**

The financial support for this study was provided by the Ankara Yıldırım Beyazıt University, Scientific Research Project, number: FDK-2023-2528.

# REFERENCES

[1] A.D. Terna, E.E. Elemike, J.I. Mbonu, O.E. Osafile, R.O. Ezeani, The future of semiconductors nanoparticles: Synthesis, properties and applications, (2021). https://doi.org/10.1016/j.mseb.2021.115363.

[2] John Vernon, Electrical and Magnetic Properties, in: Introduction to Engineering Materials, Palgrave Macmillan, London, 1992: pp. 167–179.

[3] M.E. Abdelhamid, A.P. O'mullane, G.A. Snook, Storing energy in plastics: a review on conducting polymers & their role in electrochemical energy storage, (2015). https://doi.org/10.1039/c4ra15947k.

[4] A.K. Mishra, P. Singh, D. Zala, N. Shaikh, S.K. Vemuri, J. Suthar, V. Shah, I. Mukhopadhyay, A. Ray, Plasmonic Solar Energy Harvesting by ZnO Nanostructures and Their Composite Interfaces: A Review on Fundamentals, Recent Advances, and Applications, (2023). https://doi.org/10.1002/ente.202201393.

[5] A. Klein, Energy band alignment at interfaces of semiconducting oxides: A review of experimental determination using photoelectron spectroscopy and comparison with theoretical predictions by the electron affinity rule, charge neutrality levels, and the common anion rule, in: Thin Solid Films, 2012: pp. 3721–3728. https://doi.org/10.1016/j.tsf.2011.10.055.

[6] T. Shinada, S. Okamoto, T. Kobayashi, I. Ohdomari, Enhancing semiconductor device performance using ordered dopant arrays, Nature 437 (2005) 1128–1131. https://doi.org/10.1038/nature04086.

[7] V. Schmidt, J. V. Wittemann, S. Senz, U. Gósele, Silicon nanowires: A review on aspects of their growth and their electrical properties, Advanced Materials 21 (2009) 2681–2702. https://doi.org/10.1002/adma.200803754.

[8] J. Liu, X. Qian, L. Fu, Crystal Field Effect Induced Topological Crystalline Insulators in Monolayer IV-VI Semiconductors, Nano Lett 15 (2015) 2657–2661. https://doi.org/10.1021/acs.nanolett.5b00308.

[9] A. Chaves, J.G. Azadani, H. Alsalman, D.R. da Costa, R. Frisenda, A.J. Chaves, S.H. Song, Y.D. Kim, D. He, J. Zhou, A. Castellanos-Gomez, F.M. Peeters, Z. Liu, C.L. Hinkle, S.H. Oh, P.D. Ye, S.J. Koester, Y.H. Lee, P. Avouris, X. Wang, T. Low, Bandgap engineering of two-dimensional semiconductor materials, NPJ 2D Mater Appl 4 (2020). https://doi.org/10.1038/s41699-020-00162-4.

[10] H. Takamizawa, Y. Shimizu, K. Inoue, T. Toyama, N. Okada, M. Kato, H. Uchida, F. Yano, A. Nishida, T. Mogami, Y. Nagai, Origin of characteristic variability in metal-oxide-semiconductor field-effect transistors revealed by three-dimensional atom imaging, Appl Phys Lett 99 (2011). https://doi.org/10.1063/1.3644960.

[11] T.H. Su, Y.J. Lin, Electrical conduction mechanisms of Au/NiO/heavily doped p-type Si memory devices, Appl Phys Lett 104 (2014). https://doi.org/10.1063/1.4871693.

[12] H.S.T.F.K.S. Akira Masago, A novel method for generating p-type wide- and ultrawide-bandgap III-nitride by doping with magnetic elements, Applied Physics Express 14 (2021).

[13] D. Li, M. Chen, Z. Sun, P. Yu, Z. Liu, P.M. Ajayan, Z. Zhang, Two-dimensional non-volatile programmable p-n junctions, Nat Nanotechnol 12 (2017) 901–906. https://doi.org/10.1038/nnano.2017.104.

[14] A. Abun Amanu, Electronic Electrical Conductivity in N-type Silicon, American Journal of Physics and Applications 4 (2016) 5. https://doi.org/10.11648/j.ajpa.20160401.12.

[15] X.D.J.H.C.M.L. Yi Cui, ChemInform Abstract: Doping and Electrical Transport in Silicon Nanowires, Journal Physics and Chemicals 31 (2010).

[16] M. Qian, D. Shan, Y. Ji, D. Li, J. Xu, W. Li, K. Chen, Transition of Carrier Transport Behaviors with Temperature in Phosphorus-Doped Si Nanocrystals/SiO 2 Multilayers, (2016). https://doi.org/10.1186/s11671-016-1561-z.

[17] S. Ghayempour, M. Montazer, Ultrasound irradiation based in-situ synthesis of star-like Tragacanth gum/zinc oxide nanoparticles on cotton fabric, (2016). https://doi.org/10.1016/j.ultsonch.2016.06.019.

[18] R. Huang, S. Zhang, W. Zhang, X. Yang, Progress of zinc oxide-based nanocomposites in the textile industry, (2021). https://doi.org/10.1049/cim2.12029.

[19] Y. Yin, Y. Sun, M. Yu, X. Liu, B. Yang, D. Liu, S. Liu, W. Cao, M.N.R. Ashfold, Controlling the hydrothermal growth and the properties of ZnO nanorod arrays by pre-treating the seed layer, RSC Adv 4 (2014) 44452–44456. https://doi.org/10.1039/C4RA05008H.

[20] F.Y.L.Z.W.W. Yanli Kang, Review of ZnO-based nanomaterials in gas sensors, Solid States Ionics 360 (2021).

[21] P. Judith Perez Espitia, N. de Fátima Ferreira Soares, J. Sélia dos Reis Coimbra, N. José de Andrade, R. Souza Cruz, E. Antonio Alves Medeiros, Zinc Oxide Nanoparticles: Synthesis, Antimicrobial Activity and Food Packaging Applications, (n.d.). https://doi.org/10.1007/s11947-012-0797-6.

[22] A. Lay-Ekuakille, S. Chandra Mukhopadhyay, LNEE 75 - Wearable and Autonomous Biomedical Devices and Systems for Smart Environment, n.d.

[23] K. Cherenack, L. Van Pieterson, Smart textiles: Challenges and opportunities, J Appl Phys 112 (2012). https://doi.org/10.1063/1.4742728.

[24] E. Ismar, S. Kurşun Bahadir, F. Kalaoglu, V. Koncar, Futuristic Clothes: Electronic Textiles and Wearable Technologies, Global Challenges 4 (2020). https://doi.org/10.1002/GCH2.201900092.

[25] Y. Zheng, J. Wang, P. Yao, Formaldehyde sensing properties of electrospun NiO-doped SnO 2 nanofibers, Sensors and Actuators B 156 (2011) 723–730. https://doi.org/10.1016/j.snb.2011.02.026.

[26] H.C. Su, T.T. Tran, W. Bosze, N. V. Myung, Chemiresistive sensor arrays for detection of air pollutants based on carbon nanotubes functionalized with

porphyrin and phthalocyanine derivatives, Sensors and Actuators Reports 2 (2020). https://doi.org/10.1016/j.snr.2020.100011.

[27] A.A. Trul, V.P. Chekusova, M.S. Polinskaya, A.N. Kiselev, E. V. Agina, S.A. Ponomarenko, NH3 and H2S real-time detection in the humid air by two-layer Langmuir-Schaefer OFETs, Sens Actuators B Chem 321 (2020). https://doi.org/10.1016/j.snb.2020.128609.

[28] N. Nasiri, C. Clarke, Nanostructured Gas Sensors for Medical and Health Applications: Low to High Dimensional Materials, (2019). https://doi.org/10.3390/bios9010043.

[29] G.B.S. Vladimir E. Bochenkov, Sensitivity, selectivity, and stability of gas-sensitive metal-oxide nanostructures, in: Y.-B.H. A. Umar (Ed.), Metal Oxide Nanostructures and Their Applications, American Scientific Publishers, 2010: pp. 31–52.

[30] N. Goel, K. Kunal, A. Kushwaha, M. Kumar, Metal oxide semiconductors for gas sensing, Engineering Reports 5 (2023) e12604. https://doi.org/10.1002/ENG2.12604.

[31] H. Zhang, Y. Guo, F. Meng, Metal Oxide Semiconductor Sensors for Triethylamine Detection: Sensing Performance and Improvements, Chemosensors 10 (2022). https://doi.org/10.3390/chemosensors10060231.

[32] J. Gan, J. Zhang, M.-F. Ge, X. Tu, Designs of Compliant Mechanism-Based Force Sensors: A Review, IEEE Sens J 22 (2022). https://doi.org/10.1109/JSEN.2022.3161963.

[33] J. Bosco, B. Rayappan, Gas sensing mechanism of metal oxides: The role of ambient atmosphere, type of semiconductor and gases-A review, (2015) https://www.researchgate.net/publication/270587471.

[34] M. Latino, G. Neri, CHEMORESISTIVE METAL OXIDE GAS SENSOR: WORKING PRINCIPLES AND APPLICATIONS, 98 (2021) 41. https://doi.org/10.1478/AAPP.98S1A41.

[35] A. Dey, Semiconductor metal oxide gas sensors: A review A R T I C L E I N F O, (2018). https://doi.org/10.1016/j.mseb.2017.12.036.

[36] B. Saruhan, R. Lontio Fomekong, S. Nahirniak, Review: Influences of Semiconductor Metal Oxide Properties on Gas Sensing Characteristics, Frontiers in Sensors 2 (2021). https://doi.org/10.3389/fsens.2021.657931.

[37] F. Sarf, Metal Oxide Gas Sensors by Nanostructures, (2019). www.intechopen.com.

[38] G.F. Fine, L.M. Cavanagh, A. Afonja, R. Binions, Metal Oxide Semi-Conductor Gas Sensors in Environmental Monitoring, Sensors 10 (2010) 5469–5502. https://doi.org/10.3390/s100605469.

[39] Z. Li, H. Li, Z. Wu, M. Wang, J. Luo, H. Torun, P. Hu, C. Yang, M. Grundmann, X. Liu, Y. Fu, Advances in designs and mechanisms of semiconducting metal oxide nanostructures for high-precision gas sensors operated at room temperature, Mater Horiz 6 (2019) 470–506. https://doi.org/10.1039/c8mh01365a.

[40] X. Liu, W. Zheng, R. Kumar, M. Kumar, J. Zhang, Conducting polymer-based nanostructures for gas sensors, (2022). https://doi.org/10.1016/j.ccr.2022.214517.

[41] Y.-L. Lee, C.-Y. Sheu, H. Hsiao, Gas sensing characteristics of copper phthalocyanine films: effects of film thickness and sensing temperature, Sensors and Actuators B 99 (2004) 281–287. https://doi.org/10.1016/j.snb.2003.11.024.

[42] Z. Li, S. Yan, M. Sun, H. Li, Z. Wu, J. Wang, W. Shen, Y.Q. Fu, Significantly enhanced temperature-dependent selectivity for NO 2 and H 2 S detection based on In 2 O 3 nano-cubes prepared by CTAB assisted solvothermal process, (2019). https://doi.org/10.1016/j.jallcom.2019.152518.

[43] H. Bian, S. Ma, A. Sun, X. Xu, G. Yang, S. Yan, J. Gao, Z. Zhang, H. Zhu, Improvement of acetone gas sensing performance of ZnO nanoparticles, (2015). https://doi.org/10.1016/j.jallcom.2015.09.217.

[44] A. Altındal, Ö. Kurt, A.S.¸ Engül, Ö. Bekaro˘ Glu, Kinetics of CO 2 adsorption on ball-type dicopper phthalocyanine thin film, Sensors and Actuators B 202 (2014) 373–381. https://doi.org/10.1016/j.snb.2014.05.107.

[45] Z.S. Ali, A.M. Shano, The Influence of Solvents on Polyaniline Nanofibers Synthesized by a Hydrothermal Method and their Application in Gas Sensors, (n.d.). https://doi.org/10.1007/s11664-020-08277-6.

[46] X. Liu, K. Pan, L. Wang, C. Dong, X. Xiao, Y. Wang, Butane detection: W-doped TiO2 nanoparticles for a butane gas sensor with high sensitivity and fast response/recovery, RSC Adv 5 (2015) 96539–96546. https://doi.org/10.1039/C5RA20886F.

[47] T. Itoh, I. Matsubara, J. Tamaki, K. Kanematsu, W. Shin, N. Izu, M. Nishibori, Effect of High-Humidity Aging on Performance of Tungsten Oxide-Type Aromatic Compound Sensors, 2012.

[48] R.L. Fomekong, B. Saruhan, Influence of humidity on NO2-sensing and selectivity of spray-CVD grown ZnO thin film above 400 °C, Chemosensors 7 (2019) 1–12. https://doi.org/10.3390/CHEMOSENSORS7030042.

[49] J.-H. Cho, J.-B. Yu, J.-S. Kim, S.-O. Sohn, D.-D. Lee, J.-S. Huh, Sensing behaviors of polypyrrole sensor under humidity condition, Sensors and Actuators B 108 (2005) 389–392. https://doi.org/10.1016/j.snb.2004.12.082.

[50] I.-K. Cheng, C.-Y. Lin, F.-M. Pan, Gas sensing behavior of ZnO toward H 2 at temperatures below 300 • C and its dependence on humidity and Pt-decoration, (2020). https://doi.org/10.1016/j.apsusc.2020.148551.

[51] K. Govardhan, A. Nirmala Grace, Metal/metal oxide doped semiconductor based metal oxide gas sensors - A review, Sens Lett 14 (2016) 741–750. https://doi.org/10.1166/SL.2016.3710.

[52] B. Lyson-Sypien, A. Czapla, M. Lubecka, P. Gwizdz, K. Schneider, K. Zakrzewska, K. Michalow, T. Graule, A. Reszka, M. Rekas, A. Lacz, M. Radecka, Nanopowders of chromium doped TiO 2 for gas sensors, Sensors and Actuators B 175 (2012) 163–172. https://doi.org/10.1016/j.snb.2012.02.051.

[53] A.I. Khudiar, A.M. Oufi, Influence of the aluminium doping on the physical and gas sensing properties of SnO 2 for H 2 gas detection, (2021). https://doi.org/10.1016/j.snb.2021.129633.

[54] W. Zeng, T. Liu, Z. Wang, Impact of Nb doping on gas-sensing performance of TiO 2 thick-film sensors, Sensors and Actuators B 166 (2012) 141–149. https://doi.org/10.1016/j.snb.2012.02.016.

[55] P. Nakarungsee, S. Srirattanapibul, C. Issro, I.M. Tang, S. Thongmee, High performance Cr doped ZnO by UV for NH3 gas sensor, Sens Actuators A Phys 314 (2020). https://doi.org/10.1016/j.sna.2020.112230.

[56] T. Lin, X. Lv, S. Li, Q. Wang, The morphologies of the semiconductor oxides and their gas-sensing properties, Sensors (Switzerland) 17 (2017). https://doi.org/10.3390/s17122779.

[57] X. Zhang, R. Gu, J. Zhao, G. Jin, M. Zhao, Y. Xue, Effects of Particle Size on the Gas Sensitivity and Catalytic Activity of In2O3, J Mater Eng Perform 24 (2015) 3815–3819. https://doi.org/10.1007/s11665-015-1698-4.

[58] Y.-L. Lee, W.-C. Tsai, J.-R. Maa, Effects of substrate temperature on the ®lm characteristics and gas-sensing properties of copper phthalocyanine ®lms, (n.d.).

[59] M.A. Han, H.-J. Kim, H.C. Lee, J.-S. Park, H.-N. Lee, Effects of porosity and particle size on the gas sensing properties of SnO 2 films, (2019). https://doi.org/10.1016/j.apsusc.2019.03.043.

[60] H. Adnan Banimuslem, B.Y. Kadem, Fluorinated Chromium Phthalocyanine Thin Films: Characterization and Ammonia Vapor Detection, (2018). https://doi.org/10.3390/chemosensors6040063.

[61] O. Singh, M.P. Singh, N. Kohli, R.C. Singh, Effect of pH on the morphology and gas sensing properties of ZnO nanostructures, Sensors and Actuators B 166 (2012) 438–443. https://doi.org/10.1016/j.snb.2012.02.085.

[62] R. Viter, I. Iatsunskyi, Metal Oxide Nanostructures in Sensing, in: Nanomaterials Design for Sensing Applications, Elsevier, 2019: pp. 41–91. https://doi.org/10.1016/B978-0-12-814505-0.00002-3.

[63] A. Helwig, G. Müller, G. Sberveglieri, M. Eickhoff, On the Low-Temperature Response of Semiconductor Gas Sensors, J Sens (2009) 17. https://doi.org/10.1155/2009/620720.

[64] C. Wang, L. Yin, L. Zhang, D. Xiang, R. Gao, Metal oxide gas sensors: Sensitivity and influencing factors, Sensors 10 (2010) 2088–2106. https://doi.org/10.3390/s100302088.

[65] G. Korotcenkov, B.K. Cho, Engineering approaches for the improvement of conductometric gas sensor parameters: Part 1. Improvement of sensor sensitivity and selectivity (short survey), Sens Actuators B Chem 188 (2013) 709–728. https://doi.org/10.1016/j.snb.2013.07.101.

[66] M.M. Arafat, B. Dinan, S.A. Akbar, A.S.M.A. Haseeb, Gas Sensors Based on One Dimensional Nanostructured Metal-Oxides: A Review, Sensors 12 (2012) 7207–7258. https://doi.org/10.3390/s120607207.

[67] V. Gerbreders, M. Krasovska, E. Sledevskis, A. Gerbreders, I. Mihailova, E. Tamanis, A. Ogurcovs, Hydrothermal synthesis of ZnO nanostructures with controllable morphology change, CrystEngComm 22 (2020) 1346–1358. https://doi.org/10.1039/c9ce01556f.

[68] S. Komarneni, Nanophase materials by hydrothermal, microwave-hydrothermal and microwave-solvothermal methods, 2003. https://about.jstor.org/terms.

[69] İ. Akçakoca, M. Karayazıcı, G. Topateş, Effect of processing parameters on the morphology of hydrothermally synthesized calcium borate powders, Journal of the American Ceramic Society 106 (2023) 3188–3198. https://doi.org/10.1111/jace.18972.

[70] S. Rajamanickam, S.M. Mohammad, Z. Hassan, Effect of zinc acetate dihydrate concentration on morphology of ZnO seed layer and ZnO nanorods grown by

hydrothermal method, Colloids and Interface Science Communications 38 (2020). https://doi.org/10.1016/j.colcom.2020.100312.

[71] B.S. Sannakashappanavar, N.A. Pattanashetti, C.R. Byrareddy, A.B. Yadav, Study of annealing effect on the growth of ZnO nanorods on ZnO seed layers, in: AIP Conf Proc, American Institute of Physics Inc., 2018. https://doi.org/10.1063/1.5029653.

[72] Q. Niu, R. Xue, J. Su, R. Sun, H. Yan, H. Zhang, Synthesize of ZnO Nanorods on Quartz Substrates with Seed Layer via Hydrothermal Method: Influence of Solution Concentration, Materials Sciences and Applications 13 (2022) 587–594. https://doi.org/10.4236/msa.2022.1312036.

[73] L. Zhu, Y. Xiang, Y. Liu, K. Geng, R. Yao, B. Li, Comparison of piezoelectric responses of flexible tactile sensors based on hydrothermally-grown ZnO nanorods on ZnO seed layers with different thicknesses, Sens Actuators A Phys 341 (2022). https://doi.org/10.1016/j.sna.2022.113552.

[74] N. Bhattarai, S. Wang, Q. Xu, Z. Dong, X. Chang, Y. Jiang, H. Zheng, Sources of gaseous NH3 in urban Beijing from parallel sampling of NH3 and NH4+, their nitrogen isotope measurement and modeling, Science of the Total Environment 747 (2020). https://doi.org/10.1016/j.scitotenv.2020.141361.

[75] U. Choudhari, S. Jagtap, A panoramic view of NOx and NH3 gas sensors, Nano-Structures and Nano-Objects 35 (2023). https://doi.org/10.1016/j.nanoso.2023.100995.

[76] D.S. Jyethi, Air quality: Global and regional emissions of particulate matter, SOx, and NOx, in: Plant Responses to Air Pollution, Springer Singapore, 2016: pp. 5–19. https://doi.org/10.1007/978-981-10-1201-3_2.

[77] Q. Shi, W. Wang, M. Chen, H. Zhang, S. Xu, Ammonia induces Treg/Th1 imbalance with triggered NF-κB pathway leading to chicken respiratory inflammation response, Science of the Total Environment 659 (2019) 354–362. https://doi.org/10.1016/j.scitotenv.2018.12.375.

[78] S. Huang, J. Wang, Y. Li, J. Tang, X. Zhang, Microstructure characterization and formation mechanism of colloid palladium for activation treatment on the surface of PPTA fibers, (2020). https://doi.org/10.1016/j.apsusc.2020.146134.

[79] S. Roth, M. Burghammer, A. Janotta, C. Riekel, Rotational disorder in poly(p-phenylene terephthalamide) fibers by X-ray diffraction with a 100 nm beam, Macromolecules 36 (2003) 1585–1593. https://doi.org/10.1021/ma021514g.

[80] M.A. Chowdhury, N. Hossain, M.B.A. Shuvho, M.A. Kowser, M.A. Islam, M.R. Ali, Y.A. EI-Badry, Z.M. EI-Bahy, Improvement of interfacial adhesion performance of the kevlar fiber mat by depositing SiC/TiO2/Al2O3/graphene nanoparticles, Arabian Journal of Chemistry 14 (2021). https://doi.org/10.1016/j.arabjc.2021.103406.

[81] S.-J. Park, M.-K. Seo, T.-J. Ma, D.-R. Lee, Effect of Chemical Treatment of Kevlar Fibers on Mechanical Interfacial Properties of Composites, J Colloid Interface Sci 252 (2002) 249–255. https://doi.org/10.1006/jcis.2002.8479.

[82] D. Li, Z. Guo, Metal-organic framework superhydrophobic coating on Kevlar fabric with efficient drag reduction and wear resistance, Appl Surf Sci 443 (2018) 548–557. https://doi.org/10.1016/j.apsusc.2018.03.030.

[83] Z. Lu, W. Hu, F. Xie, Y. Hao, Highly improved mechanical strength of aramid paper composite via a bridge of cellulose nanofiber, Cellulose 24 (2017) 2827–2835. https://doi.org/10.1007/s10570-017-1315-9.

[84] M. Bulut, M. Alsaadi, A. Erkliğ, A comparative study on the tensile and impact properties of Kevlar, carbon, and S-glass/epoxy composites reinforced with SiC particles, Mater Res Express 5 (2018). https://doi.org/10.1088/2053-1591/aaa991.

[85] C. Jia, P. Chen, W. Liu, B. Li, Q. Wang, Surface treatment of aramid fiber by air dielectric barrier discharge plasma at atmospheric pressure, Appl Surf Sci 257 (2011) 4165–4170. https://doi.org/10.1016/j.apsusc.2010.11.190.

[86] L. Liu, Y.D. Huang, Z.Q. Zhang, Z.X. Jiang, L.N. Wu, Ultrasonic treatment of aramid fiber surface and its effect on the interface of aramid/epoxy composites,

Appl Surf Sci 254 (2008) 2594–2599. https://doi.org/10.1016/j.apsusc.2007.09.091.

[87] X. Yang, Q. Tu, X. Shen, M. Pan, C. Jiang, P. Zhu, Y. Li, P. Li, C. Hu, Surface modification of Poly(p-phenylene terephthalamide) fibers by polydopamine-polyethyleneimine/graphene oxide multilayer films to enhance interfacial adhesion with rubber matrix, Polym Test 78 (2019). https://doi.org/10.1016/j.polymertesting.2019.105985.

[88] C.X. Wang, M. Du, J.C. Lv, Q.Q. Zhou, Y. Ren, G.L. Liu, D.W. Gao, L.M. Jin, Surface modification of aramid fiber by plasma induced vapor phase graft polymerization of acrylic acid. I. Influence of plasma conditions, Appl Surf Sci 349 (2015) 333–342. https://doi.org/10.1016/j.apsusc.2015.05.036.

[89] E.G. Chatzi, J.L. Koenig, Morphology and structure of kevlar fibers: A review, Polym Plast Technol Eng 26 (1987) 229–270. https://doi.org/10.1080/03602558708071938.

[90] A.M. Issam, A new approach to obtain Kevlar-49 from PET waste bottles, Research on Chemical Intermediates 40 (2014) 3033–3044. https://doi.org/10.1007/s11164-013-1149-5.

[91] A. Almaroof, A. Ali, F. Mannocci, S. Deb, Semi-interpenetrating network composites reinforced with Kevlar fibers for dental post fabrication, Dent Mater J 38 (2019) 511–521. https://doi.org/10.4012/dmj.2018-040.

[92] A. Engelbrecht-Wiggans, F. Burni, E. Guigues, S. Jiang, T.Q. Huynh, Z. Tsinas, D. Jacobs, A.L. Forster, Effects of temperature and humidity on high-strength p-aramid fibers used in body armor, Textile Research Journal 90 (2020) 2428–2440. https://doi.org/10.1177/0040517520918232.

[93] M.B. Ibrahim, H.Y. Habib, R.M. Jabrah, Preparation of kevlar-49 Fabric/E-glass fabric/epoxy composite materials and characterization of their mechanical properties, Revue Des Composites et Des Materiaux Avances 30 (2020) 133–141. https://doi.org/10.18280/rcma.303-403.

[94] D. Puchowicz, M. Cieslak, Raman Spectroscopy in the Analysis of Textile Structures, (2021) www.intechopen.com.

[95] G.C. Rutledge, U.W. Suter', C.D. Papaspyrides, Analysis zyxwvu of Structure and Polymorphism in zyx Poly@-phenyleneterephthalamide) through Correlation of Simulation and Experiment, 1991.

[96] K. Haijuan, S. Hui, C. Jin, D. Haiquan, D. Xiaoma, Q. Mengmeng, Y. Muhuo, Z. Youfeng, Improvement of Adhesion of Kevlar Fabrics to Epoxy by Surface Modification With Acetic Anhydride in Supercritical Carbon Dioxide, (2018). https://doi.org/10.1002/pc.25100.

[97] T. Ma, Y. Zhao, K. Ruan, X. Liu, J. Zhang, Y. Guo, X. Yang, J. Kong, J. Gu, Highly Thermal Conductivities, Excellent Mechanical Robustness and Flexibility, and Outstanding Thermal Stabilities of Aramid Nanofiber Composite Papers with Nacre-Mimetic Layered Structures, ACS Appl Mater Interfaces 12 (2020) 1677–1686. https://doi.org/10.1021/acsami.9b19844.

[98] D. Ahmed, Z. Hongpeng, K. Haijuan, L. Jing, M. Yu, Y. Muhuo, Microstructural developments of poly (p-phenylene terephthalamide) fibers during heat treatment process: A review, Materials Research 17 (2014) 1180–1200. https://doi.org/10.1590/1516-1439.250313.

[99] R. Fernandes Nascimento, A. Oliveira da Silva, R. Pondé Weber, S. Neves Monteiro, Influence of UV radiation and moisten associated with natural weathering on the ballistic performance of aramid fabric armor, (2020). https://doi.org/10.1016/j.jmrt.2020.07.046.

[100] G. Zheng, R. Jianhua, R. Guo, Nickel deposition on Kevlar fabric modified with aminopropyltrimethoxysilane in supercritical fluid via electroless plating, Journal of Materials Science: Materials in Electronics 29 (2018) 19200–19206. https://doi.org/10.1007/s10854-018-0046-5.

[101] A.M. Bochek, Effect of Hydrogen Bonding on Cellulose Solubility in Aqueous and Nonaqueous Solvents, Nauka/Interperiodica] Russian Journal of Applied Chemistry 76 (2003) 1761–1770.

[102] S. Chabi, D.A. Dikin, J. Yin, S. Percec, F. Ren, Structure-Mechanical Property Relations of Skin-Core Regions of Poly(p-phenylene terephthalamide) Single Fiber, (n.d.). https://doi.org/10.1038/s41598-018-37366-0.

[103] Y. Lv, Z. Zhang, J. Yan, W. Zhao, C. Zhai, J. Liu, Growth mechanism and photoluminescence property of hydrothermal oriented ZnO nanostructures evolving from nanorods to nanoplates, J Alloys Compd 718 (2017) 161–169. https://doi.org/10.1016/j.jallcom.2017.05.075.

[104] S. Guillemin, V. Consonni, E. Appert, E. Puyoo, L. Rapenne, H. Roussel, Critical nucleation effects on the structural relationship between ZnO seed layer and nanowires, Journal of Physical Chemistry C 116 (2012) 25106–25111. https://doi.org/10.1021/jp308643w.

[105] Q. Zhang, M. Honda, Y. Ichikawa, Seed layer morphology influencing on ZnO nanorod growth by hydrothermal synthesis, n.d.

[106] D. Byrne, E. McGlynn, M.O. Henry, K. Kumar, G. Hughes, A novel, substrate independent three-step process for the growth of uniform ZnO nanorod arrays, in: Thin Solid Films, 2010: pp. 4489–4492. https://doi.org/10.1016/j.tsf.2009.12.014.

[107] J.E. Boercker, J.B. Schmidt, E.S. Aydil, Transport limited growth of zinc oxide nanowires, Cryst Growth Des 9 (2009) 2783–2789. https://doi.org/10.1021/cg900021u.

[108] J. Song, S. Lim, Effect of seed layer on the growth of ZnO nanorods, Journal of Physical Chemistry C 111 (2007) 596–600. https://doi.org/10.1021/jp0655017.

[109] S. Anas, S. Rahul, K.B. Babitha, R. V. Mangalaraja, S. Ananthakumar, Microwave accelerated synthesis of zinc oxide nanoplates and their enhanced photocatalytic activity under UV and solar illuminations, Appl Surf Sci 355 (2015) 98–103. https://doi.org/10.1016/j.apsusc.2015.07.058.

[110] G.H. Mhlongo, D.E. Motaung, F.R. Cummings, H.C. Swart, S. Ray, A highly responsive NH 3 sensor based on pd-loaded Zno nanoparticles prepared via a

chemical precipitation approach, (2019). https://doi.org/10.1038/s41598-019-46247-z.

[111] D.K. Chaudhary, Y.S. Maharjan, S. Shrestha, S. Maharjan, S.P. Shrestha, L.P. Joshi, Sensing Performance of a ZnO-based Ammonia Sensor, Journal of Physical Science 33 (2022) 97–108. https://doi.org/10.21315/jps202.33.1.7.

[112] S. Goutham, K.K. Sadasivuni, D. Santhosh Kumar, K.V. Rao, Flexible ultra-sensitive and resistive NO 2 gas sensor based on nanostructured Zn (x) Fe (1Àx)2 O 4, (2018). https://doi.org/10.1039/c7ra10478b.

[113] P. Srinivasan, J. Bosco, B. Rayappan, Growth of Eshelby twisted ZnO nanowires through nanoflakes & nanoflowers: A room temperature ammonia sensor, (2018). https://doi.org/10.1016/j.snb.2018.09.003.

[114] T.-Y. Chen, H.-I. Chen, C.-S. Hsu, C.-C. Huang, J.-S. Wu, P.-C. Chou, W.-C. Liu, Characteristics of ZnO nanorods-based ammonia gas sensors with a cross-linked configuration, Sensors and Actuators B 221 (2015) 491–498. https://doi.org/10.1016/j.snb.2015.06.122.

[115] G.K. Mani, J. Bosco, B. Rayappan, A highly selective room temperature ammonia sensor using spray deposited zinc oxide thin film, Sensors and Actuators B 183 (2013) 459–466. https://doi.org/10.1016/j.snb.2013.03.132.

[116] X. Li, J. Wang, One-dimensional and two-dimensional synergized nanostructures for high-performing energy storage and conversion, InfoMat 2 (2020) 3–32. https://doi.org/10.1002/INF2.12040.

[117] X. Zhao, B. Cai, Q. Tang, Y. Tong, Y. Liu, One-dimensional nanostructure field-effect sensors for gas detection, Sensors (Switzerland) 14 (2014) 13999–14020. https://doi.org/10.3390/s140813999.

[118] M. Shooshtari, A. Salehi, S. Vollebregt, Effect of temperature and humidity on the sensing performance of TiO2nanowire-based ethanol vapor sensors, Nanotechnology 32 (2021). https://doi.org/10.1088/1361-6528/abfd54.

[119] J. Xuan, G. Zhao, M. Sun, F. Jia, X. Wang, T. Zhou, G. Yin, B. Liu, Low-temperature operating ZnO-based NO 2 sensors: a review, (2020). https://doi.org/10.1039/d0ra07328h.

[120] Y. Zou, S. Chen, J. Sun, J. Liu, Y. Che, X. Liu, J. Zhang, D. Yang, Highly efficient gas sensor using a hollow SnO2 microfiber for triethylamine detection, ACS Sens 2 (2017) 897–902. https://doi.org/10.1021/acssensors.7b00276.

[121] Y.-J. Jeong, C. Balamurugan, D.-W. Lee, Enhanced CO 2 gas-sensing performance of ZnO nanopowder by La loaded during simple hydrothermal method, Sensors and Actuators B 229 (2016) 288–296. https://doi.org/10.1016/j.snb.2015.11.093.

[122] C. Wang, X. Cui, J. Liu, X. Zhou, X. Cheng, P. Sun, X. Hu, X. Li, J. Zheng, G. Lu, Design of Superior Ethanol Gas Sensor Based on Al-Doped NiO Nanorod-Flowers, ACS Sens 1 (2016) 131–136. https://doi.org/10.1021/acssensors.5b00123.

[123] J. Xu, Z. Xue, N. Qin, Z. Cheng, Q. Xiang, The crystal facet-dependent gas sensing properties of ZnO nanosheets: Experimental and computational study, Sensors and Actuators B 242 (2017) 148–157. https://doi.org/10.1016/j.snb.2016.09.193.

[124] N. Qin, Q. Xiang, H. Zhao, J. Zhang, J. Xu, Evolution of ZnO microstructures from hexagonal disk to prismoid, prism and pyramid and their crystal facet-dependent gas sensing properties, CrystEngComm 16 (2014) 7062–7073. https://doi.org/10.1039/c4ce00637b.

[125] G.-J. Li, X.-H. Zhang, S. Kawi, Relationships between sensitivity, catalytic activity, and surface areas of SnO gas sensors, Sensors and Actuators B 60 (1999) 64–70. www.elsevier.nlrlocatersensorb.

[126] A. Ajjaq, F. Bulut, O. Ozturk, S. Acar, Advanced NH3 Detection by 1D Nanostructured La:ZnO Sensors with Novel Intrinsic p-n Shifting and Ultrahigh Baseline Stability, ACS Sens 9 (2024) 895–911. https://doi.org/10.1021/acssensors.3c02256.

[127] C.-F. Li, C.-Y. Hsu, Y.-Y. Li, NH 3 sensing properties of ZnO thin films prepared via sol-gel method, (2014). https://doi.org/10.1016/j.jallcom.2014.03.120.

[128] M.Y. Al-Darwesh, S.S. Ibrahim, M. Faiad Naief, A.M. Mohammed, H. Chebbi, Synthesis and characterizations of zinc oxide nanoparticles and its ability to detect O 2 and NH 3 gases, Results Chem 6 (2023) 101064. https://doi.org/10.1016/j.rechem.2023.101064.

[129] N.A. Anasthasiya, S. Ramya, D. Balamurugan, P.K. Rai, B.G. Jeyaprakash, Adsorption property of volatile molecules on ZnO nanowires: computational and experimental approach, Bull. Mater. Sci 41 (2018) 4. https://doi.org/10.1007/s12034-017-1538-2.

[130] S. Jinn Chang, W. Yin Weng, C. Liang Hsu, T. Jen Hsueh, High sensitivity of a ZnO nanowire-based ammonia gas sensor with Pt nano-particles, Nano Commun Netw 1 (2010) 283–288. https://doi.org/10.1016/j.nancom.2010.09.005.

[131] F. Shao, J.D. Fan, F. Hernández-Ramírez, C. Fàbrega, T. Andreu, A. Cabot, J.D. Prades, N. López, F. Udrea, A. De Luca, S.Z. Ali, J.R. Morante, NH 3 sensing with self-assembled ZnO-nanowire HP sensors in isothermal and temperature-pulsed mode, Sensors and Actuators B 226 (2016) 110–117. https://doi.org/10.1016/j.snb.2015.11.109.

[132] A. Wei, Z. Wang, L.H. Pan, W.W. Li, L. Xiong, X.C. Dong, W. Huang, Room-temperature NH3 gas sensor based on hydrothermally grown ZnO nanorods, Chinese Physics Letters 28 (2011). https://doi.org/10.1088/0256-307X/28/8/080702.

[133] S. Anantachaisilp, S.M. Smith, C. Ton-That, T. Osotchan, A.R. Moon, M.R. Phillips, Tailoring deep level surface defects in ZnO nanorods for high sensitivity ammonia gas sensing, Journal of Physical Chemistry C 118 (2014) 27150–27156. https://doi.org/10.1021/jp5085857.

[134] G. Konuk Ege, Ö. Akay, H. Yüce, A chemosensitive-based ammonia gas sensor with PANI/PEO–ZnO nanofiber composites sensing layer, Microelectronics International (2023). https://doi.org/10.1108/MI-04-2023-0051.